Mathematics

https://www.aimspress.com/journal/Math

AIMS Mathematics, 10(9): 22150–22179.
DOI: 10.3934/math.2025986
Received: 29 June 2025
Revised: 22 August 2025
Accepted: 10 September 2025
Published: 24 September 2025

Research article

Exploring chaotic behavior, conservation laws, Lie symmetry, and soliton dynamics in the generalized $A\mp$ equation

Beenish[1,*] **and Fehaid Salem Alshammari**[2]

[1] Department of Mathematics, Quaid-I-Azam University 45320, Islamabad, Pakistan; Beenish@math.qau.edu.pk

[2] Department of Mathematics and Statistics, College of Science, Imam Mohammad Ibn Saud Islamic University (IMSIU), Riyadh, Saudi Arabia; falshammari@imamu.edu.sa

* **Correspondence:** Email: Beenish@math.qau.edu.pk.

Abstract: In this study, the generalized $A\mp$ equation is explored, with symmetry generators addressing the criteria for Lie invariance. The proposed approach yields the Lie algebra, where translation symmetries in space and time correspond to mass conservation and energy conservation, respectively. By employing Lie group methods, the generalized $A\mp$ equation is transformed through suitable similarity transformations into a system of highly nonlinear ordinary differential equations. The modified F-expansion approach is then applied to derive soliton solutions. The behavior of these solutions is visualized in three and two dimensions (3D and 2D), with contour plots, and the effect of wave speed is studied for specific values of the physical components in the equation. These results contribute significantly to advancing the field by enhancing the depth and impact of research. Subsequently, the dynamic behavior of the model was thoroughly investigated, with particular emphasis on the chaos analysis. The incorporation of an external periodic force led to the emergence of chaotic and quasi-periodic phenomena. These complex dynamics were illustrated using time series plots, 2D and 3D phase portraits, return maps, bifurcation diagrams, chaotic attractors, fractal dimensions, Poincaré maps, and Lyapunov exponent analysis. This comprehensive approach not only provides deeper insight into the system's stability and sensitivity but also offers a valuable framework for identifying and controlling complex behaviors in nonlinear dynamic models.

Keywords: conservation laws; multistability; Hamilton function; fractal dimension; soliton solution
Mathematics Subject Classification: 26A48, 26A51, 33B10, 37K40, 39B62

1. Introduction

In the upcoming year, nonlinear partial differential equations (NLPDEs) are expected to play a significant role in modeling various phenomena across disciplines such as physics, chemistry, biology, engineering, and finance [1, 2]. For instance, in biology, NLPDEs can model tumors' growth dynamics, while in finance, they provide more accurate frameworks for pricing derivatives like options and warrants. Their applications in physics are particularly broad, spanning areas like fluid mechanics, quantum mechanics, and plasma physics [3, 4]. NLPDEs are also widely employed to simulate nonlinear phenomena across several scientific and technological domains [5–7]. Notable examples include the Heisenberg ferromagnet-type model [8], the stochastic potential Korteweg-de Vries equation [9], and the fractional Chen–Lee–Liu equation [10]. Over recent years, researchers worldwide have introduced numerous methodologies to explore the dynamics of NLPDEs. As a result, various analytical techniques have been developed, including the generalized Arnous framework [11], and the Kumar-Malik method [12] among others [14–16].

This article investigates the generalized A∓ equation, which exhibits a wide spectrum of soliton types and structures. The equation is further extended to a more general form to encompass broader dynamic features [17]:

$$(\Psi^3)_{\mathrm{ttt}} - 2(\Psi^3)_{\varsigma\varsigma\varsigma} + \Psi_\varsigma(\Gamma\Psi\Psi_{\varsigma\varsigma} + \mathfrak{B}(\Psi_\varsigma)^2 + \Upsilon + \kappa\Psi^4) = 0. \tag{1.1}$$

Here, $\Upsilon, \kappa, \mathfrak{B} \in \Re$, $\Psi(\varsigma, \mathrm{t})$ is the dependent variable, while ς represents the spatial variable and t denotes the temporal variable. We refer to Eq (1.1) as the generalized A± equation. Notably, when $\Gamma = 54$, $\mathfrak{B} = 3, \Upsilon = \mp 3\Upsilon^2$, and $\kappa = \pm 3$, Eq (1.1) reduces to Alexeyev's A∓ equation, whose integrability and soliton solutions have been studied in the following form [17]:

$$(\Psi^3)_{\mathrm{ttt}} - 2(\Psi^3)_{\varsigma\varsigma\varsigma} + 3\Psi_\varsigma(18\Gamma\Psi\Psi_{\varsigma\varsigma} + (\Psi_\varsigma)^2 \mp \Upsilon^2 \mp 3\Psi^4) = 0. \tag{1.2}$$

Yan Zhou et al. [17] worked on Eq (1.1), conducting a bifurcation analysis and obtaining exact traveling wave solutions using the complete discriminant method. Compared with the A± equation Eq (1.2), the generalized form Eq (1.1) incorporates a broader set of parameters, suggesting a richer spectrum of solutions and dynamic properties. In this research, we analyze Eq (1.1) from four different perspectives.

- First, we investigate the Lie point symmetries of Eq (1.1), which helps reduce the differential equations, leading to exact solutions and invariant forms.
- Second, we derive the conservation laws of Eq (1.1).
- Third, we obtain soliton solutions of Eq (1.1) using the modified F-expansion method.
- Last, we perform a chaos analysis of Eq (1.1). We apply a transformation to convert the ordinary differential equation (ODE) into a dynamic system, then introduce perturbation terms. Our investigation elucidates the presence of chaotic and quasi-periodic phenomena, which we substantiate through the use of various analytical instruments:
- Bifurcation diagrams facilitate the monitoring of behavioral alterations within the system as the parameters fluctuate, thereby elucidating transitions towards chaotic states.
- The fractal dimension serves to quantify the complexity inherent in the system while differentiating chaotic motion from regular trajectories.
- Lyapunov exponents provide a metric for the system's sensitivity to the initial conditions, which is a fundamental hallmark of chaotic behavior.

- Chaotic attractors graphically represent the long-term dynamics of the system, unveiling trajectories that, while irregular, remain bounded.
- Poincaré maps transform continuous dynamics into discrete intersections, thereby underscoring both periodic and chaotic regimes.
- Return maps scrutinize the recurrence characteristics, enabling use to distinguish stable, periodic, and chaotic motion.
- Two-dimensional (2D) and three-dimensional (3D) phase portraits illustrate the trajectories of the system, revealing patterns of divergence or convergence.
- Multistability analysis investigates the simultaneous existence of multiple stable states contingent upon varying initial conditions.
- Time-series analysis assesses the evolution of signals, effectively identifying irregular oscillations that typify chaotic behavior. These analytical tools collectively furnish a robust framework for the identification and comprehension of chaotic dynamics as described in Eq (1.1).

Symmetry analysis can be traced back to the contributions of Sophus Lie (1842–1899), who pioneered Lie group theory as a systematic approach to the examination of differential equations [14]. His seminal work expanded upon classical concepts of symmetry, thereby laying the groundwork for the development of Lie point symmetries and their associated transformations within the realm of modern mathematics. Over the years, methodologies rooted in symmetry have found extensive application across various domains, including engineering and nonlinear scientific inquiry. The importance of symmetry analysis is underscored by its capacity to facilitate the simplification of differential equations, either by diminishing their order or by converting them into forms that are amenable to analytical resolution [18]. This analytical framework not only fosters the identification of exact solutions but also contributes to the systematic classification of differential equations while elucidating the conservation principles as articulated by Noether's theorem (1918). Additionally, symmetry methods are integral to the fields of integrability, stability analysis, and perturbation theory, with particular relevance to the study of nonlinear dynamical systems [19, 20]. The applications of symmetry analysis are diverse, encompassing areas such as fluid dynamics, plasma physics, relativity, optics, quantum mechanics, and financial mathematics. It serves as a powerful instrument for modeling phenomena such as wave propagation, solitons, and chaotic systems, thereby affirming its status as a vital resource in contemporary theoretical and applied sciences [21–23].

Conservation laws play a crucial role in integrability, numerical method development, and analyzing the behavior of solutions for differential equations in nonlinear phenomena. A well-established approach for determining the conservation laws of partial differential equation (PDE) is Noether's theorem [24], which is closely associated with the existence of a classical Lagrangian. However, some differential equations, such as scalar evolution equations, do not possess a Lagrangian formulation [25]. To address this, various alternative methods have been developed, including the multiplier method, the direct method, partial Lagrangian method, and the non-local conservation method [26].

In 1834, John Scott Russell [27] first identified solitons while observing a solitary wave generated by a canal boat that stopped abruptly. This wave traveled for miles without dissipating or losing its shape, leading Russell to name it a "soliton". A soliton is a unique traveling wave that, even after colliding with another soliton, retains its original form. Solitons are solutions of PDEs that describe various physical phenomena, including water waves and wave propagation in weakly anharmonic mass-spring chains. Their defining characteristic is the presence of exponential tails, which allow their solutions to be expressed using exponential functions. Additionally, solitons follow a superposition-like principle, meaning they pass through one another without alteration. Further developments include theories on dispersion-managed solitons and quasi-linear pulses. In optical communication systems, dark solitons are known to be more stable in noisy environments and experience slower dispersion under loss conditions compared with bright solitons. In this paper, we employ the modified F-expansion technique and highlight its advantages, including its efficiency in obtaining exact solutions, its adaptability to various nonlinear equations, and its ability to generate diverse wave structures. The modified F-expansion technique presents significant benefits owing to its capacity to produce an extensive array of precise solutions, encompassing solitons and periodic waves, that are pertinent to nonlinear differential equations. It offers a methodical and unambiguous framework, thereby diminishing computational intricacies. Furthermore, it effectively incorporates a variety of nonlinearities and parameter fluctuations, thereby augmenting its relevance to intricate physical models [28–32].

The article is structured as follows: Section 2 explores Lie point symmetries, the symmetry group of the generalized A∓ equation, and similarity reductions. Section 3 derives the conservation laws, while Section 4 examines localized wave structures. Section 5 analyzes the physical behavior of the solutions, and Section 6 discusses the chaotic characteristics. Section 7 discuss the analytical tools for detecting chaos analysis. Section 8 presents the conclusions.

2. Insights from symmetry analysis

In this section, we discuss the results of Eq (1.1) to determine the Lie point symmetries, the symmetry groups, and equation reduction using similarity variables.

Theorem 1. *Equation* (1.1) *possesses a 2D Lie algebra generated by translation symmetries.*

Proof. Consider a one-parameter local Lie group of transformations involving the variables ς, t, and Ψ, defined as follows [14]:

$$\begin{aligned} \varsigma^* &= \varsigma + \vartheta_0 \sigma_1(\varsigma, \mathrm{t}, \Psi) + O(\vartheta_0^2), \\ \mathrm{t}^* &= \mathrm{t} + \vartheta_0 \sigma_2(\varsigma, \mathrm{t}, \Psi) + O(\vartheta_0^2), \\ \Psi^* &= \Psi + \vartheta_0 \Delta(\varsigma, \mathrm{t}, \Psi) + O(\vartheta_0^2). \end{aligned} \tag{2.1}$$

Here, $\vartheta_0 \in \mathbb{R}$ represents the group parameter. The corresponding vector field Ξ for the equation is given by

$$\Xi = \sigma_1(\varsigma, \mathrm{t}, \Psi)\frac{\partial}{\partial \varsigma} + \sigma_2(\varsigma, \mathrm{t}, \Psi)\frac{\partial}{\partial \mathrm{t}} + \Delta(\varsigma, \mathrm{t}, \Psi)\frac{\partial}{\partial \Psi}. \tag{2.2}$$

Applying the $\Xi^{(3)}$ to Eq (1.1), we have

$$\Xi^{(3)}((\Psi^3)_{\mathrm{ttt}} - 2(\Psi^3)_{\varsigma\varsigma\varsigma} + \Psi_\varsigma(\Gamma\Psi\Psi_{\varsigma\varsigma} + \mathfrak{B}(\Psi_\varsigma)^2 + \Upsilon + \kappa\Psi^4) = 0.)|_{Eq\ (1.1)=0} = 0. \tag{2.3}$$

After simplifying Eq (2.3), we obtain the following equation:

$$\Xi^{(3)}(\kappa\Psi^4\Psi_\varsigma - \mathfrak{B}(\Psi^3)_\varsigma + \Gamma\Psi\Psi_\varsigma\Psi_{\varsigma\varsigma} + 3\Psi^2\Psi_{\mathrm{t}} - 6\Psi^2\Psi_{\varsigma\varsigma\varsigma} - 36\Psi\Psi_\varsigma\Psi_{\varsigma\varsigma} - 12(\Psi^3)_\varsigma + \Gamma\Psi_\varsigma)|_{Eq\ (1.1)=0} = 0. \tag{2.4}$$

The third-order extension $\Xi^{(3)}$ is defined as follows:

$$\mathcal{P}r^{[3]}\Xi = \Xi + \Delta^{\mathrm{t}}\frac{\partial}{\partial \Psi} + \Delta^{\varsigma}\frac{\partial}{\partial \Psi_\varsigma} + \Delta^{\varsigma\varsigma}\frac{\partial}{\partial \Psi_{\varsigma\varsigma}} + \Delta^{\varsigma\varsigma\varsigma}\frac{\partial}{\partial \Psi_{\varsigma\varsigma\varsigma}}\cdot \tag{2.5}$$

We also have the corresponding coefficients

$$\begin{cases}\Delta^{\mathrm{t}} = \mathcal{D}_{\mathrm{t}}(\Delta) - \Psi_{\varsigma}\mathcal{D}_{\mathrm{t}}(\sigma_1) - \Psi_{\mathrm{t}}\mathcal{D}_{\mathrm{t}}(\sigma_2),\\ \Delta^{\varsigma} = \mathcal{D}_{\varsigma}(\Delta) - \Psi_{\varsigma}\mathcal{D}_{\varsigma}(\sigma_1) - \Psi_{\mathrm{t}}\mathcal{D}_{\varsigma}(\sigma_2),\\ \Delta^{\varsigma\varsigma} = \mathcal{D}_{\varsigma}(\Delta^{\varsigma}) - \Psi_{\varsigma\varsigma}\mathcal{D}_{\varsigma}(\sigma_1) - \Psi_{\mathrm{t}\varsigma}\mathcal{D}_{\varsigma}(\sigma_2),\\ \Delta^{\varsigma\varsigma\varsigma} = \mathcal{D}_{\varsigma}(\Delta^{\varsigma\varsigma}) - \Psi_{\varsigma\varsigma\varsigma}\mathcal{D}_{\varsigma}(\sigma_1) - \Psi_{\mathrm{t}\varsigma\varsigma}\mathcal{D}_{\varsigma}(\sigma_2),\\ \Delta^{\varsigma\varsigma\varsigma\varsigma} = \mathcal{D}_{\varsigma}(\Delta^{\varsigma\varsigma\varsigma}) - \Psi_{\varsigma\varsigma\varsigma}\mathcal{D}_{\varsigma}(\sigma_1) - \Psi_{\mathrm{t}\varsigma\varsigma\varsigma}\mathcal{D}_{\varsigma}(\sigma_2).\end{cases} \tag{2.6}$$

The operators $\mathcal{D}_{\mathrm{t}}$ and $\mathcal{D}_{\varsigma}$ represent the total derivatives with respect to time and space, respectively. Utilizing the third-order extension and substituting the values of Δ^{t}, Δ^{ς}, $\Delta^{\varsigma\varsigma}$, and $\Delta^{\varsigma\varsigma\varsigma}$, we obtain

$$\begin{aligned}
&18\Psi^3\frac{\partial\sigma_2}{\partial\Psi} = 0,\ 18\Psi^3\frac{\partial\sigma_2}{\partial\varsigma} = 0,\ 18\Psi^3\frac{\partial^2\sigma_2}{\partial\varsigma^2} = 0,\ 36\Psi^3\frac{\partial^2\sigma_1}{\partial\Psi^2} = 0,\ 18\frac{\partial\sigma_1}{\partial\Psi}\Psi^3 = 0,\\
&18\Psi^3\frac{\partial^2\sigma_2}{\partial\Psi^2} + 72\frac{\partial\sigma_2}{\partial\Psi}\Psi^2 - 2\frac{\partial\sigma_2}{\partial\Psi}\Gamma\Psi^2 = 0,\ 18\Psi^3\frac{\partial^2\sigma_2}{\partial\varsigma\partial\Psi} + 36\frac{\partial\sigma_2}{\partial\varsigma}\Psi^2 - \frac{\partial\sigma_2}{\partial\varsigma}\Gamma\Psi^2 = 0,\\
&36\Psi^3\frac{\partial^2\sigma_2}{\partial\varsigma\partial\Psi} + 72\frac{\partial\sigma_2}{\partial\varsigma}\Psi^2 - 2\frac{\partial\sigma_2}{\partial\varsigma}\Gamma\Psi^2 = 0,\ -\frac{\partial\sigma_2}{\partial\Psi}\Gamma\Psi^2 + 18\Psi^3\frac{\partial^2\sigma_2}{\partial\Psi^2} + 36\frac{\partial\sigma_2}{\partial\Psi}\Psi^2 = 0,\\
&18\Psi^3\frac{\partial^3\sigma_2}{\partial\varsigma^2\partial\Psi} + 9\frac{\partial\sigma_1}{\partial\Psi}\Psi^3 + 36\frac{\partial^2\sigma_2}{\partial\varsigma^2}\Psi^2 - \frac{\partial^2\sigma_2}{\partial\varsigma^2}\Gamma\Psi^2 = 0,\\
&\frac{\partial\Delta}{\partial\varsigma}\Upsilon\Psi + \frac{\partial\Delta}{\partial\varsigma}\kappa\Psi^5 - 6\Psi^3\frac{\partial^3\Delta}{\partial\varsigma^3} + 3\frac{\partial\Delta}{\partial\mathrm{t}}\Psi^3 = 0.
\end{aligned} \tag{2.7}$$

This system (2.7) can be solved either manually or using software such as Maple using the Gem package. By solving the system (2.7), we obtain the infinitesimals

$$\Delta = 0,\ \sigma_2 = \mathfrak{C}_1,\ \sigma_1 = \mathfrak{C}_2, \tag{2.8}$$

where $\mathfrak{C}_1$ and $\mathfrak{C}_2$ are arbitrary constants. Consequently, the Lie algebra of translational symmetry for Eq (1.1) is spanned by two vector fields

$$\Xi_1 = \frac{\partial}{\partial\mathrm{t}},\ \ \Xi_2 = \frac{\partial}{\partial\varsigma}\cdot \tag{2.9}$$

□

2.1. *Applying Lie symmetry reduction to the Eq* (1.1)

This section focuses on obtaining exact solutions for the generalized $A\mp$ equation using the Lie symmetry method. First, PDEs are reduced to ODEs via Lie symmetry, and then an appropriate technique is applied to solve them. The reduction process involves the subalgebras Ξ_1 and Ξ_2.

Condition a. $\Xi_1 = \frac{\partial}{\partial\mathrm{t}}$.

The characteristic equation derived from Ξ_1 is

$$\frac{d\mathrm{t}}{1} = \frac{d\varsigma}{0} = \frac{d\Psi}{0}. \tag{2.10}$$

As a result, we arrive at the transformation

$$\Psi = \Phi_0(\mathcal{R}), \quad \mathcal{R} = \varsigma\cdot \tag{2.11}$$

By inserting the expressions for $\Psi_\varsigma, \Psi_{\varsigma\varsigma}, \Psi_{\varsigma\varsigma\varsigma}$, and Ψ_{t} and into Eq (1.1), we get

$$12(\Phi_0')^3 - 36\Phi_0\Phi_0'\Phi_0'' - 6\Phi_0^2\Phi_0''' + \Gamma\Phi_0\Phi_0'\Phi_0'' + (\Phi_0')^3\mathfrak{B} + \Upsilon\Phi_0' + \kappa\Phi_0^4\Phi_0' = 0. \tag{2.12}$$

Condition b. $\Xi_2 = \frac{\partial}{\partial\varsigma}$.
The equation characterizing Ξ_2 takes the form

$$\frac{d\mathrm{t}}{0} = \frac{d\varsigma}{1} = \frac{d\Psi}{0}. \tag{2.13}$$

This leads to the following transformation

$$\Psi = \Phi_1(\mathcal{R}), \quad \mathcal{R} = \mathrm{t}\cdot \tag{2.14}$$

Plugging the computed values of $\Psi_\varsigma, \Psi_{\varsigma\varsigma}, \Psi_{\varsigma\varsigma\varsigma}$, and Ψ_{t} into Eq (1.1), we derive

$$3\Phi_1^2(\Phi_1') = 0. \tag{2.15}$$

From the solution of Eq (2.15), we obtain the trivial solution

$$\Phi_1 = \mathfrak{U}_1\cdot \tag{2.16}$$

Applying the backward transformation (2.14), we obtain the solution of Eq (1.1)

$$\Psi(\varsigma, \mathrm{t}) = \mathfrak{U}_1. \tag{2.17}$$

Condition c. $\Xi_1 + \mu_1\Xi_2 = \frac{\partial}{\partial \mathrm{t}} + \mu_1\frac{\partial}{\partial\varsigma}$.
The equation characterizing $\Xi_1 + \mu_1\Xi_2$ takes the form

$$\frac{d\mathrm{t}}{1} = \frac{d\varsigma}{\mu_1} = \frac{d\Psi}{0}. \tag{2.18}$$

This leads to the following transformation

$$\Psi(\varsigma, \mathrm{t}) = \mathcal{V}(\mathcal{R}), \quad \mathcal{R} = \varsigma - \mu_1\mathrm{t}, \tag{2.19}$$

where μ_1 shows the wave speed. By substituting Eq (2.19) into Eq (1.1), with the condition $\Gamma = 2\mathfrak{B}$, we transform the PDE into an ODE in terms of $\mathcal{V}(\mathcal{R})$

$$-3\mathcal{V}^2\mathcal{V}'\mu_1 - 12(\mathcal{V}')^3 - 36\mathcal{V}\mathcal{V}'\mathcal{V}'' - 6\mathcal{V}^2\mathcal{V}''' + 2\mathcal{V}'\mathfrak{B}\mathcal{V}\mathcal{V}'' + \mathfrak{B}(\mathcal{V}')^3 + \mathcal{V}'\Upsilon + \mathcal{V}'\kappa\mathcal{V}^4 = 0\cdot \tag{2.20}$$

Integrating Eq (2.20) once concerning $\mathcal{R}$, and setting the integration constant to zero, we obtain the final reduced equation for $\mathcal{V}(\mathcal{R})$

$$\frac{1}{5}\mathcal{V}^5\kappa - \mu_1\mathcal{V}^3 + \mathcal{V}\Upsilon + (\mathcal{V}')^2\mathfrak{B}\mathcal{V} - 12\mathcal{V}\mathcal{V}'^2 - 6\mathcal{V}^2\mathcal{V}'' = 0\cdot \tag{2.21}$$

3. Conservation laws of Eq (1.1)

Conservation laws constitute a pivotal element in the examination of dynamic systems and are thoroughly implemented across a multitude of scientific disciplines. These principles articulate essential physical characteristics of PDEs that characterize a variety of natural phenomena. Historically, their origins can be traced to classical mechanics, wherein they regulated the conservation of energy, momentum, and mass, the subsequently extending their influence to fluid dynamics, electromagnetism, and quantum mechanics [24]. In contemporary applications, conservation laws assist in evaluating the integrability and linearization of PDEs, in facilitating the derivation of first integrals for ODEs, and in the identification of potential functions. They also enable the development of non-locally connected systems and enhance the precision of numerical simulations. Within the realm of engineering, they contribute to the refinement of computational models of fluid dynamics , thereby ensuring stability and accuracy in simulations. In the field of plasma physics, these laws are instrumental in the analysis of wave propagation and energy transfer phenomena [33, 34].

3.1. Review of the multiplier approach to identify conserved quantities

Here, we present an in-depth explanation of the multiplier approach [24].

Step 1. Suppose we are dealing with an s-order PDE:

$$\Im(\varsigma, \Psi, \Psi_1, \Psi_2, ..., \Psi_s) = 0\cdot \tag{3.1}$$

In this expression, Ψ is the dependent variable, $\varsigma = (\varsigma^1, \varsigma^2, \varsigma^3, ..., \varsigma^m)$ indicates the set of independent variables, and Ψ_1 and Ψ_s correspond to the first- and sth-order derivatives of Ψ with respect to ς .

Step 2. The form of the Euler operator is given by

$$\frac{\delta}{\delta\Psi} = \frac{\partial}{\partial\Psi} - \mathcal{D}_p \frac{\partial}{\partial\Psi_p} + \mathcal{D}_{pq} \frac{\partial}{\partial\Psi_{pq}} - \mathcal{D}_{pqm} \frac{\partial}{\partial\Psi_{pqm}} + ...\cdot \tag{3.2}$$

Step 3. The total derivative operator can be written as

$$\mathcal{D}_p = \frac{\partial}{\partial\varsigma^p} + \Psi_p \frac{\partial}{\partial\Psi} + \Psi_{pq} \frac{\partial}{\partial\Psi_q} + ..., \ 1 \ \leq \ p \ \leq n. \tag{3.3}$$

It acts as a derivative operator concerning space and time.

Step 4. Assuming the s-tuple $\Omega = (\Omega^1, \Omega^2, \Omega^3, \Omega^4, ..., \Omega^p)$, we have:

$$\mathcal{D}_p \Omega^p = 0, \quad 1 \ \leq \ p \ \leq n. \tag{3.4}$$

Satisfaction of all conditions in Eq (3.1) implies that Eq (3.4) represents a local conservation law.

Step 5. The multiplier $\varkappa(\varsigma, \mathrm{t}, \Psi)$ related to Eq (3.1) is defined such that it satisfies the condition

$$\mathcal{D}_p \Omega^p = \varkappa \mathrm{H}, \tag{3.5}$$

for any function Ψ defined over the variables $(\varsigma^1, \varsigma^2, \varsigma^3, ..., \varsigma^s)$.

Step 6. Taking the derivative of Eq (3.5) leads to the determining equations for the multiplier $\varkappa(\varsigma, \mathrm{t}, \Psi)$

$$\frac{\delta}{\delta\Psi}(\varkappa \mathrm{H}) = 0\cdot \tag{3.6}$$

Eq (3.6) is formulated for any function $\Psi(\varsigma^1, \varsigma^2, \varsigma^3, \varsigma^4, ..., \varsigma^s)$, not only for those satisfying Eq (3.1).
Step 7. Once the multipliers $\varkappa(\varsigma, \mathrm{t}, \Psi)$ are obtained from Eq (3.6), Eq (3.5) is used to determine the conservation laws.

Theorem 2. Eq (1.1) permits the presence of local conservation laws:

$$\begin{cases} \mathcal{D}_{\varsigma}(\varphi_{\varsigma}^1) + \mathcal{D}_{\mathrm{t}}(\varphi_{\mathrm{t}}^1) = 0, \\ \mathcal{D}_{\varsigma}(\varphi_{\varsigma}^2) + \mathcal{D}_{\mathrm{t}}(\varphi_{\mathrm{t}}^2) = 0, \end{cases} \tag{3.7}$$

where φ_{ς}^1, φ_{ς}^2, φ_{t}^1, and φ_{t}^2 are defined as follows:

$$\begin{aligned}
\varphi_{\mathrm{t}}^1 &= \frac{36\Pi_1}{54 - \Gamma + \Pi_1},\ \varphi_{\mathrm{t}}^2 = \frac{-36\Psi^{\frac{-\Gamma}{12} + \frac{9}{2} - \frac{\Pi_1}{12}}}{\Gamma - 54 + \Pi_1},\ \Pi_1 = \sqrt{\Gamma^2 + 48\mathfrak{B} - 60\Gamma + 324},\ \Pi_2 = \Psi^{\frac{-\Gamma}{12} + \frac{3}{2} + \frac{\Pi_1}{12}}, \\
\varphi_{\varsigma}^1 &= \frac{12(-\Pi_2\mathfrak{B}\Gamma\Psi_{\varsigma}^2 + \Pi_2\mathfrak{B}\Psi_{\varsigma}^2\Pi - \Pi_2\Gamma^2\Psi_{\varsigma\varsigma}^2 + \Pi_1\Pi_2\Gamma\Psi_{\varsigma\varsigma} + 78\Pi_2\mathfrak{B}\Psi_{\varsigma}^2 + 12\Pi_2\mathfrak{B}\Psi_{\varsigma}^2 - 12\Pi_1\Pi_2\Psi_{\varsigma}^2 - 24\Pi_2\mathfrak{B}\Psi_{\varsigma\varsigma}}{(78 - \Gamma + \Pi_1)(\Pi_1 - \Gamma + 30))} \\
&+ \frac{12(84\Pi_2\Gamma\Psi_{\varsigma\varsigma} - 54\Pi_1\Pi_2\Psi_{\varsigma\varsigma} - \upsilon\Pi_2\Gamma + \Upsilon\Pi_2\Pi_1 - 936\Pi_2\Psi_{\varsigma}^2 - \kappa\Pi_2\Gamma + \kappa\Psi^{\frac{13}{2} - \frac{\Gamma}{12} - \frac{\Pi_1}{12}}\Pi_1 - 1332\Psi^{\frac{7}{2} - \frac{\Gamma}{12} + \frac{\Pi_1}{12}}\Psi_{\varsigma\varsigma})}{(78 - \Gamma + \Pi_1)(\Pi_1 - \Gamma + 30)} \\
&+ \frac{12(78\Upsilon\Psi^{\frac{5}{2} - \frac{\Gamma}{12} + \frac{\Pi_1}{12}} + 30\kappa\Psi^{\frac{13}{2} - \frac{\Gamma}{12} + \frac{\Pi_1}{12}})}{(78 - \Gamma + \Pi_1)(\Pi_1 - \Gamma + 30)}, \\
\varphi_{\varsigma}^2 &= -\frac{12(\Pi_2\mathfrak{B}\Gamma\Psi_{\varsigma}^2 + \Pi_2\mathfrak{B}\Psi_{\varsigma}^2\Pi_1 + \Pi_2\Gamma^2\Psi_{\varsigma\varsigma}^2 + \Pi_1\Pi_2\Gamma\Psi_{\varsigma\varsigma} - 78\Pi_2\mathfrak{B}\Psi_{\varsigma}^2 - 12\Pi_2\Gamma\Psi_{\varsigma}^2 - 12\Pi_2\Pi_1\Psi_{\varsigma}^2 + 24\Pi_2\mathfrak{B}\Psi_{\varsigma\varsigma})}{(\Gamma - 78 + \Pi_1)(\Pi_1 + \Gamma - 30)} \\
&- \frac{12(-84\Pi_2\Gamma\Psi_{\varsigma\varsigma} - 54\Pi_1\Pi_2 + \Upsilon\Pi_2\Pi_1 + 936\Pi_2\Psi_{\varsigma}^2 + \kappa\Psi^{\frac{13}{2} - \frac{\Gamma}{12} - \frac{\Pi_1}{12}}\Gamma + \kappa\Psi^{\frac{13}{2} - \frac{\Gamma}{12} - \frac{\Pi_1}{12}}\Pi_1 + 1332\Psi^{\frac{-\Gamma}{12} + \frac{7}{2} - \frac{\Pi_1}{12}}\Psi_{\varsigma\varsigma})}{(\Gamma - 78 + \Pi_1)(\Pi_1 + \Gamma - 30)} \\
&- \frac{12(\Upsilon\Pi_2\Gamma - 78\Gamma\Psi^{\frac{13}{2} - \frac{\Gamma}{12} - \frac{\Pi_1}{12}} - 30\kappa\Psi^{\frac{13}{2} - \frac{\Gamma}{12} - \frac{\Pi_1}{12}})}{(\Gamma - 78 + \Pi_1)(\Pi_1 + \Gamma - 30)}.
\end{aligned} \tag{3.8}$$

The full set of local conservation laws for Eq (4.1) with the paramters Π_1 and Π_2 is given by $\{\varkappa_1, \varkappa_2\} = \left\{\Psi^{\frac{-\Gamma}{12} + \frac{3}{2} + \frac{\Pi_1}{12}}, \Psi^{\frac{-\Gamma}{12} + \frac{3}{2} - \frac{\Pi_1}{12}}\right\}$, fully capturing all local conservation laws of the equation.

Proof. Using the details from Eq (3.4), we derive the following system of equations:

$$\varkappa_{\Psi\Psi} = \frac{-\varkappa_{\Psi}\Gamma\Psi + 2\varkappa\mathfrak{B} + 12\varkappa_{\Psi}\Psi - \varkappa\Gamma}{6\Psi^2},\ \ \varkappa_{\mathrm{t}} = 0,\ \ \varkappa_{\varsigma} = 0\cdot \tag{3.9}$$

Consequently, the corresponding solution of Eq (3.9) is obtained as follows:

$$\varkappa = g_1\Psi^{\frac{-\Gamma}{12} + \frac{3}{2} + \frac{\Pi_1}{12}} + g_2\Psi^{\frac{-\Gamma}{12} + \frac{3}{2} - \frac{\Pi_1}{12}},\ \Pi_1 = \sqrt{\Gamma^2 + 48\mathfrak{B} - 60\Gamma + 324}\cdot \tag{3.10}$$

The constants g_i (for $i = 1, 2$) are arbitrary. The solution Eq (3.10) further confirms the validity of Theorem 2 when the conservation law multipliers are given by

$$\{\varkappa_1, \varkappa_2\} = \left\{\Psi^{-\frac{\Gamma}{12} + \frac{3}{2} + \frac{\Pi_1}{12}}, \Psi^{-\frac{\Gamma}{12} + \frac{3}{2} - \frac{\Pi_1}{12}}\right\}\cdot \tag{3.11}$$

□

4. Localized wave structures of Eq (1.1)

In this section, we investigate the localized wave structures of Eq (1.1) using the modified F-expansion method. Additionally, an overview of the modified F-expansion method is provided.

4.1. Overview of the modified F-expansion approach

This section presents the modified F-expansion method for solving nonlinear PDEs of the form

$$\mathfrak{S}(\Psi, \Psi_{\varsigma}, \Psi_{\mathrm{t}}, \Psi_{\varsigma\varsigma}, \Psi_{\varsigma\mathrm{t}}, \Psi_{\mathrm{tt}}, \Psi_{\varsigma\varsigma\varsigma}, \dots) = 0, \tag{4.1}$$

where $\mathfrak{S}$ is a polynomial in $\Psi(\varsigma, \mathrm{t})$ and its derivatives. The key steps of the approach are outlined below.
Step 1. Consider the following wave transformation.

$$\Psi(\varsigma, \mathrm{t}) = \mathcal{V}(\mathcal{R}), \ \mathcal{R} = \varsigma - \mu_1 \mathrm{t}, \tag{4.2}$$

where μ_1 shows the wave speed to be determined. When describing the dynamics of wave propagation, μ_1 is essential.
Step 2. Substituting Eq (4.2) into Eq (4.1) yields a nonlinear ODE for $\mathcal{V}(\mathcal{R})$

$$\mathfrak{R}(\mathcal{V}, \mathcal{V}', \mathcal{V}'', \mathcal{V}''', \mathcal{V}'''', ...) = 0. \tag{4.3}$$

Step 3. Assume that the solution $\mathcal{V}$ of Eq (4.3) can be represented as a finite series in the form

$$\mathcal{V}(\mathcal{R}) = s_0 + \sum_{b=1}^{\mathfrak{F}} s_b \Theta^b(\mathcal{R}) + r_0 \Theta^{-b}(\mathcal{R}) \cdot \tag{4.4}$$

Here, s_0, s_b, r_b are undetermined constants, and the right-hand side of Eq (4.4) is a polynomial in $\Theta(\mathcal{R})$, which satisfies an auxiliary ODE

$$\Theta'(\mathcal{R}) = \chi + \eta \Theta(\mathcal{R}) + \varepsilon \Theta^2(\mathcal{R}) \cdot \tag{4.5}$$

Step 4. The integer $\mathfrak{F}$ is determined by balancing the highest derivative with the nonlinear term of the highest-degree in Eq (4.3).
Step 5. Substituting Eq (4.4) into Eq (4.3) and using Eq (4.5), we collect terms with the same degree of $\Theta(\mathcal{R})$, forming a polynomial in $\Theta(\mathcal{R})$. Setting each coefficient to zero gives a system of algebraic equations for s_0, s_b, r_b, and μ_1.
Step 6. Solving the algebraic equations gives the constants s_0, s_b, r_b, and μ_1.
Step 7. The known solutions of Eq (4.5), as shown in Table 1, are then substituted into Eq (4.4), yielding more exact solutions of Eq (4.1).

Table 1. Parameter-solution relations in Eq (4.5).

Conditions on parameters	**Corresponding solutions of $\Theta(\mathcal{R})$**
$\chi = 0,\ \eta = 1,\ \epsilon = -1$	$\Theta_1(\mathcal{R}) = 0.5 + 0.5\tanh(0.5\mathcal{R})$
$\chi = 0,\ \eta = -1,\ \epsilon = 1$	$\Theta_2(\mathcal{R}) = 0.5 - 0.5\coth(0.5\mathcal{R})$
$\chi = \frac{1}{2},\ \eta = 0,\ \epsilon = -\frac{1}{2}$	$\Theta_{3a}(\mathcal{R}) = \coth(\mathcal{R}) \mp \operatorname{csch}(\mathcal{R})$ $\Theta_{3b}(\mathcal{R}) = \tanh(\mathcal{R}) \mp i\operatorname{sech}(\mathcal{R})$
$\chi = 1,\ \eta = 0,\ \epsilon = -1$	$\Theta_{4a}(\mathcal{R}) = \tanh(\mathcal{R})$ $\Theta_{4b}(\mathcal{R}) = \coth(\mathcal{R})$
$\chi = \frac{1}{2},\ \eta = 0,\ \epsilon = \frac{1}{2}$	$\Theta_{5a}(\mathcal{R}) = \sec(\mathcal{R}) + \tan(\mathcal{R})$ $\Theta_{5b}(\mathcal{R}) = \csc(\mathcal{R}) - \cot(\mathcal{R})$
$\chi = -\frac{1}{2},\ \eta = 0,\ \epsilon = -\frac{1}{2}$	$\Theta_{6a}(\mathcal{R}) = \sec(\mathcal{R}) - \tan(\mathcal{R})$ $\Theta_{6b}(\mathcal{R}) = \csc(\mathcal{R}) + \cot(\mathcal{R})$
$\chi = \pm 1,\ \eta = 0,\ \epsilon = \pm 1$	$\Theta_{7a}(\mathcal{R}) = \tan(\mathcal{R})$ $\Theta_{7b}(\mathcal{R}) = \cot(\mathcal{R})$
$\chi \neq 0,\ \eta = \epsilon = 0$	$\Theta_8(\mathcal{R}) = \mathcal{P}\mathcal{R}$
$\chi \neq 0,\ \eta \neq 0,\ \epsilon = 0$	$\Theta_9(\mathcal{R}) = \dfrac{-\mathcal{P} + \exp(\mathcal{S}\mathcal{R})}{\mathcal{S}}$

4.2. Application of modified F-expansion method on Eq (2.21)

By applying the homogeneous balancing method between $\mathcal{V}^2\mathcal{V}''$ and $\mathcal{V}^5$, the assumed solution in Eq (2.21) is truncated as follows:

$$\mathcal{V}(\mathcal{R}) = s_0 + s_1\Theta(\mathcal{R}) + \frac{r_1}{\Theta(\mathcal{R})}. \tag{4.6}$$

Equation (4.6) satisfies an auxiliary ODE:

$$\begin{aligned}
\Theta'(\mathcal{R}) &= \chi + \eta\Theta(\mathcal{R}) + \varepsilon\Theta^2(\mathcal{R}),\\
\Theta''(\mathcal{R}) &= \eta\Theta'(\mathcal{R}) + 2\varepsilon\Theta(\mathcal{R})\Theta'(\mathcal{R})\cdot
\end{aligned} \tag{4.7}$$

Substituting Eqs (4.6) and (4.7) into Eq (2.21) and setting the coefficients of $\Theta(\mathcal{R})$ to zero results in the following system of equations:

$$\begin{cases}
\mathcal{V}^{-1}(\mathcal{R}): 2\kappa s_1^2 r_1^3 - \mathfrak{B}\chi^2 s_1^2 r_1 - 4\mathfrak{B}\chi\eta s_0 s_1 r_1 - 2\mathfrak{B}\chi\epsilon s_1 r_1^2 - \mathfrak{B}\eta^2 s_1 r_1^2 + 2\mathfrak{B}\eta\epsilon s_0 r_1^2 + \mathfrak{B}\epsilon^2 r_1^3 + \kappa s_0^4 r_1 \\
\quad + 6\kappa s_0^2 s_1 r_1^2 - 12\chi\epsilon s_0^2 r_1 - 12\chi\epsilon s_1 r_1^2 - 6\eta^2 s_0^2 r_1 - 6\eta^2 s_1 r_1^2 - 36\eta\epsilon s_0 r_1^2 - 12\epsilon^2 r_1^3 - 3\mu_1 s_0^2 r_1 - 3\mu_1 s_1 r_1^2 + \Upsilon r_1 = 0, \\
\mathcal{V}^{-2}(\mathcal{R}): -2\mathfrak{B}\chi^2 s_0 s_1 r_1 - 2\mathfrak{B}\chi\eta s_1 r_1^2 + 2\mathfrak{B}\chi\epsilon s_0 r_1^2 + \mathfrak{B}\eta^2 s_0 r_1^2 + 2\mathfrak{B}\eta\epsilon r_1^3 + 2\kappa s_0^3 r_1^2 + 4\kappa s_0 s_1 r_1^3 \\
\quad - 18\chi\eta s_0^2 r_1 - 18\chi\eta s_1 r_1^2 - 48\chi\epsilon s_0 r_1^2 - 24\eta^2 s_0 r_1^2 - 30\eta\epsilon r_1^3 - 3\mu_1 s_0 r_1^2 = 0, \\
\mathcal{V}^{-3}(\mathcal{R}): -\mathfrak{B}\chi^2 s_1 r_1^2 + 2\mathfrak{B}\chi\eta s_0 r_1^2 + 2\mathfrak{B}\chi\epsilon r_1^3 + \mathfrak{B}\eta^2 r_1^3 + 2\kappa s_0^2 r_1^3 + \kappa s_1 r_1^4 \\
\quad - 12\chi^2 s_0^2 r_1 - 12\chi^2 s_1 r_1^2 - 60\chi\eta s_0 r_1^2 - 36\chi\epsilon r_1^3 - 18\eta^2 r_1^3 - \mu_1 r_1^3 = 0, \\
\mathcal{V}^{-4}(\mathcal{R}): \mathfrak{B}\chi^2 s_0 r_1^2 + 2\mathfrak{B}\chi\eta r_1^3 + \kappa s_0 r_1^4 - 36\chi^2 s_0 r_1^2 - 42\chi\eta r_1^3 = 0, \\
\mathcal{V}^{-5}(\mathcal{R}): \mathfrak{B} r_1^3\chi^2 + \tfrac{1}{5}\kappa r_1^5 - 24 r_1^3\chi^2 = 0, \\
\mathcal{V}^{0}(\mathcal{R}): 4\kappa s_0^3 s_1 r_1 + 6\kappa s_0 s_1^2 r_1^2 - 6\mu_1 s_0 s_1 r_1 + \mathfrak{B} s_1^2 s_0\chi^2 - 12 r_1^2 s_0\epsilon^2 - 6 s_0^2 s_1\eta\chi - 6 s_1^2 r_1\eta\chi + \Upsilon s_0 \\
\quad - 12 s_1^2 s_0\chi^2 - 6 s_1 r_1^2\eta\epsilon - 6 s_0^2 r_1\eta\epsilon + \mathfrak{B} r_1^2 s_0\epsilon^2 + \tfrac{1}{5}\kappa s_0^5 - \mu_1 s_0^3 - 2\mathfrak{B} s_1^2 r_1\chi\eta - 2\mathfrak{B} s_1 r_1^2\eta\epsilon \\
\quad - 2\mathfrak{B} s_1 r_1 s_0\eta^2 - 4\mathfrak{B} s_1 r_1 s_0\chi\epsilon = 0, \\
\mathcal{V}^{1}(\mathcal{R}): \mathfrak{B}\chi^2 s_1^3 + 2\mathfrak{B}\chi\eta s_0 s_1^2 - 2\mathfrak{B}\chi\epsilon s_1^2 r_1 - \mathfrak{B}\eta^2 s_1^2 r_1 - 4\mathfrak{B}\eta\epsilon s_0 s_1 r_1 - \mathfrak{B}\epsilon^2 s_1 r_1^2 + \kappa s_0^4 s_1 \\
\quad + 6\kappa s_0^2 s_1^2 r_1 + 2\kappa s_1^3 r_1^2 - 12\chi^2 s_1^3 - 36\chi\eta s_0 s_1^2 - 12\chi\epsilon s_0^2 s_1 - 12\chi\epsilon s_1^2 r_1 - 6\eta^2 s_0^2 s_1 - 6\eta^2 s_1^2 r_1 \\
\quad - 3\mu_1 s_0^2 s_1 - 3\mu_1 s_1^2 r_1 + \Upsilon s_1 = 0, \\
\mathcal{V}^{2}(\mathcal{R}): 2\mathfrak{B}\chi\eta s_1^3 + 2\mathfrak{B}\chi\epsilon s_0 s_1^2 + \mathfrak{B}\eta^2 s_0 s_1^2 - 2\mathfrak{B}\eta\epsilon s_1^2 r_1 - 2\mathfrak{B}\epsilon^2 s_0 s_1 r_1 + 2\kappa s_0^3 s_1^2 + 4\kappa s_0 s_1^3 r_1 \\
\quad - 30\chi\eta s_1^3 - 48\chi\epsilon s_0 s_1^2 - 24\eta^2 s_0 s_1^2 - 18\eta\epsilon s_0^2 s_1 - 18\eta\epsilon s_1^2 r_1 - 3\mu_1 s_0 s_1^2 = 0, \\
\mathcal{V}^{3}(\mathcal{R}): 2\mathfrak{B}\chi\epsilon s_1^3 + \mathfrak{B}\eta^2 s_1^3 + 2\mathfrak{B}\eta\epsilon s_0 s_1^2 - \mathfrak{B}\epsilon^2 s_1^2 r_1 + 2\kappa s_0^2 s_1^3 + \kappa s_1^4 r_1 - 36\chi\epsilon s_1^3 - 18\eta^2 s_1^3 \\
\quad - 60\eta\epsilon s_0 s_1^2 - 12\epsilon^2 s_0^2 s_1 - 12\epsilon^2 s_1^2 r_1 - \mu_1 s_1^3 = 0, \\
\mathcal{V}^{4}(\mathcal{R}): 2\mathfrak{B}\eta\epsilon s_1^3 + \mathfrak{B}\epsilon^2 s_0 s_1^2 + \kappa s_0 s_1^4 - 42\eta\epsilon s_1^3 - 36\epsilon^2 s_0 s_1^2 = 0, \\
\mathcal{V}^{5}(\mathcal{R}): \mathfrak{B} s_1^3\epsilon^2 - 24 s_1^3\epsilon^2 + \tfrac{1}{5}\kappa s_1^5 = 0.
\end{cases}$$

By solving the algebraic system (4.2) using Maple, we obtain the following values

$$\begin{cases}
\kappa = \dfrac{5(\mathfrak{B}-24)(16\mathfrak{B}\chi^2\epsilon^2 - 8\mathfrak{B}\chi\eta^2\epsilon + \mathfrak{B}\eta^4 - 192\chi^2\epsilon^2 + 96\chi\eta^2 - 12\eta^4)}{16\Upsilon}, \ \mathfrak{B} \neq 24, 12\,, \\
\Upsilon = \Upsilon, \ \mu_1 = 2\chi\epsilon\mathfrak{B} - \dfrac{\mathfrak{B}\eta^2}{2} - 36\epsilon\chi + 9\eta^2, \ r_1 = 0, \ s_0 = \dfrac{2\eta\sqrt{\Upsilon}}{(4\chi\epsilon - \eta^2)\sqrt{12-\mathfrak{B}}}, \\
s_1 = \dfrac{2\epsilon\sqrt{\Upsilon}}{(4\chi\epsilon - \eta^2)\sqrt{12-\mathfrak{B}}}.
\end{cases} \tag{4.8}$$

Utilizing Eqs (4.6) and (4.8) about the solution sets under the various conditions specified in Eq (4.7), the solutions of Eq (1.1) are given as follows.
For $\chi = 0,\ \eta = 1,\ \epsilon = -1$, and $\mathfrak{B} \neq 12$, the solution of Eq (2.21) and Eq (1.1) is obtained as follows:

$$\begin{cases} \mathcal{V}_1(\mathcal{R}) = \dfrac{-2\sqrt{\Upsilon}}{\sqrt{12-\mathfrak{B}}} - \dfrac{2\epsilon\sqrt{\Upsilon}(0.5+0.5\tanh(0.5(\mathcal{R})))}{\sqrt{12-\mathfrak{B}}}. \\ \Psi_1(\varsigma,\mathrm{t}) = \dfrac{-2\sqrt{\Upsilon}}{\sqrt{12-\mathfrak{B}}} - \dfrac{2\epsilon\sqrt{\Upsilon}(0.5+0.5\tanh\left(0.5(\varsigma-(-\frac{\mathfrak{B}}{2}+9)\mathrm{t})\right))}{\sqrt{12-\mathfrak{B}}}. \end{cases} \tag{4.9}$$

A solution to Eqs (1.1) and (2.21) is obtained under the conditions $\chi = 0,\ \eta = -1,\ \epsilon = 1$, and $\mathfrak{B} \neq 12$

$$\begin{cases} \mathcal{V}_2(\mathcal{R}) = \dfrac{-2\sqrt{\Upsilon}}{\sqrt{12-\mathfrak{B}}} + \dfrac{2\sqrt{\Upsilon}(0.5-0.5\coth(0.5\mathcal{R}))}{\sqrt{12-\mathfrak{B}}}. \\ \Psi_2(\varsigma,\mathrm{t}) = \dfrac{-2\sqrt{\Upsilon}}{\sqrt{12-\mathfrak{B}}} + \dfrac{2\sqrt{\Upsilon}(0.5-0.5\coth\left(0.5(\varsigma-(\frac{\mathfrak{B}}{2}-9)\mathrm{t})\right))}{\sqrt{12-\mathfrak{B}}}. \end{cases} \tag{4.10}$$

Under the specific conditions $\chi = 0.5,\ \eta = 0,\ \epsilon = -0.5$, and $\mathfrak{B} \neq 12$, Eqs (1.1) and (2.21) admit a solution

$$\begin{cases} \mathcal{V}_{3a}(\mathcal{R}) = \dfrac{\sqrt{\Upsilon}(\coth(\mathcal{R}) \mp \operatorname{csch}(\mathcal{R}))}{\sqrt{12-\mathfrak{B}}}. \\ \Psi_{3a}(\varsigma,\mathrm{t}) = \dfrac{\sqrt{\Upsilon}(\coth(\varsigma-(\frac{\mathfrak{B}}{2}-9)\mathrm{t}) \mp \operatorname{csch}(\varsigma-(\frac{\mathfrak{B}}{2}-9)\mathrm{t}))}{\sqrt{12-\mathfrak{B}}}. \\ \mathcal{V}_{3b}(\mathcal{R}) = \dfrac{\sqrt{\Upsilon}(\tanh(\mathcal{R}) \mp i\operatorname{sech}(\mathcal{R}))}{\sqrt{12-\mathfrak{B}}}. \\ \Psi_{3b}(\varsigma,\mathrm{t}) = \dfrac{\sqrt{\Upsilon}(\tanh(\varsigma-(\frac{\mathfrak{B}}{2}-9)\mathrm{t}) \mp i\operatorname{sech}(\varsigma-(\frac{\mathfrak{B}}{2}-9)\mathrm{t}))}{\sqrt{12-\mathfrak{B}}}. \end{cases} \tag{4.11}$$

Setting $\chi = 1,\ \eta = 0,\ \epsilon = -1$, and $\mathfrak{B} \neq 12$, leads to a solution of Eqs (1.1) and (2.21)

$$\begin{cases} \mathcal{V}_{4a}(\mathcal{R}) = \dfrac{\sqrt{\Upsilon}\tanh(\mathcal{R})}{2\sqrt{12-\mathfrak{B}}}. \\ \Psi_{4a}(\varsigma,\mathrm{t}) = \dfrac{\sqrt{\Upsilon}\tanh(\varsigma-(36-2\mathfrak{B})\mathrm{t})}{2\sqrt{12-\mathfrak{B}}}. \\ \mathcal{V}_{4b}(\mathcal{R}) = \dfrac{\sqrt{\Upsilon}\coth(\mathcal{R})}{2\sqrt{12-\mathfrak{B}}}. \\ \Psi_{4b}(\varsigma,\mathrm{t}) = \dfrac{\sqrt{\Upsilon}\coth(\varsigma-(36-2\mathfrak{B})\mathrm{t})}{2\sqrt{12-\mathfrak{B}}}. \end{cases} \tag{4.12}$$

Imposing the constraints $\chi = 0.5,\ \eta = 0,\ \epsilon = 0.5$, and $\mathfrak{B} \neq 12$, we derive a solution for Eqs (1.1) and (2.21)

$$\begin{cases} \mathcal{V}_{5a}(\mathcal{R}) = \dfrac{\sqrt{\Upsilon}(\sec(\mathcal{R}) + \tan(\mathcal{R}))}{\sqrt{12 - \mathfrak{B}}}. \\ \Psi_{5a}(\varsigma, \mathrm{t}) = \dfrac{\sqrt{\Upsilon}(\sec(\varsigma - (\frac{\mathfrak{B}}{2} - 9)\mathrm{t}) + \tan(\varsigma - (\frac{\mathfrak{B}}{2} - 9)\mathrm{t}))}{\sqrt{12 - \mathfrak{B}}}. \\ \mathcal{V}_{5b}(\mathcal{R}) = \dfrac{\sqrt{\Upsilon}(\csc(\mathcal{R}) - \cot(\mathcal{R}))}{\sqrt{12 - \mathfrak{B}}}. \\ \Psi_{5b}(\varsigma, \mathrm{t}) = \dfrac{\sqrt{\Upsilon}(\csc(\varsigma - (\frac{\mathfrak{B}}{2} - 9)\mathrm{t}) - \cot(\varsigma - (\frac{\mathfrak{B}}{2} - 9)\mathrm{t}))}{\sqrt{12 - \mathfrak{B}}}. \end{cases} \tag{4.13}$$

Given $\chi = -0.5,\ \eta = 0,\ \epsilon = -0.5$, and $\mathfrak{B} \neq 12$, it follows that Eqs (1.1) and (2.21) have a solution

$$\begin{cases} \mathcal{V}_{6a}(\mathcal{R}) = \dfrac{-\sqrt{\Upsilon}(\sec(\mathcal{R}) - \tan(\mathcal{R}))}{\sqrt{12 - \mathfrak{B}}}. \\ \Psi_{6a}(\varsigma, \mathrm{t}) = \dfrac{-\sqrt{\Upsilon}(\sec(\varsigma - (\mathfrak{B} - 36)\mathrm{t}) - \tan(\varsigma - (\mathfrak{B} - 36)\mathrm{t}))}{\sqrt{12 - \mathfrak{B}}}. \\ \mathcal{V}_{6b}(\mathcal{R}) = \dfrac{-\sqrt{\Upsilon}(\csc(\mathcal{R}) + \cot(\mathcal{R}))}{\sqrt{12 - \mathfrak{B}}}. \\ \Psi_{6b}(\varsigma, \mathrm{t}) = \dfrac{-\sqrt{\Upsilon}(\csc(\varsigma - (\mathfrak{B} - 36)\mathrm{t}) + \cot(\varsigma - (\mathfrak{B} - 36)\mathrm{t}))}{\sqrt{12 - \mathfrak{B}}}. \end{cases} \tag{4.14}$$

When the parameters satisfy $\chi = \pm 1,\ \eta = 0,\ \epsilon = \pm 1$, and $\mathfrak{B} \neq 12$, Eqs (1.1) and (2.21) produce a solution

$$\begin{cases} \mathcal{V}_{7a}(\mathcal{R}) = \dfrac{\mp 2\sqrt{\Upsilon}\tan(\mathcal{R})}{\sqrt{12 - \mathfrak{B}}}. \\ \Psi_{7a}(\varsigma, \mathrm{t}) = \dfrac{\mp 2\sqrt{\Upsilon}\tan(\varsigma - \mu_1\mathrm{t})}{\sqrt{12 - \mathfrak{B}}}. \\ \mathcal{V}_{7b}(\mathcal{R}) = \dfrac{\mp 2\sqrt{\Upsilon}\cot(\mathcal{R})}{\sqrt{12 - \mathfrak{B}}}. \\ \Psi_{7b}(\varsigma, \mathrm{t}) = \dfrac{\mp 2\sqrt{\Upsilon}\cot(\varsigma - \mu_1\mathrm{t})}{\sqrt{12 - \mathfrak{B}}}. \end{cases} \tag{4.15}$$

5. Wave behavior visualization

Visualizing the results through multiple graphical techniques enables a deeper understanding of waves' characteristics and their behavior under varying conditions. Surface plots effectively demonstrate the spatial distribution and evolution of wave patterns, while contour plots highlight key amplitude and intensity variations. A 3D graphical approach, enriched with color-coded elements, provides a clear representation of how the spatial and temporal dimensions interact. In this section, specific physical parameters have been chosen to explore the correlation between the newly derived soliton solutions and the governing equation. To further examine the effects of parameters ς and $\mathfrak{t}$, we utilize 3D, 2D, and contour plots. Figures 1–5 offer a detailed depiction of the behavior of dark, bright-dark, and periodic waves, as well as kink and anti-kink solitons.

In Figure 1(a)–(c), the wave behavior of the solution $\Psi_1(\varsigma, \mathfrak{t})$ is illustrated by choosing the parameter values $\Upsilon = 0.78$ and $\mathfrak{B} = 1.23$, with the domain of ς and $\mathfrak{t}$ set as $(-4.4, 4.4)$. For a positive wave speed of 8.385, the solution exhibits a kink soliton. In Figure 1(b), we use the same parameter values but fix $\varsigma = 1.45$ to obtain a 2D plot. On the other hand, in Figure 2(a)–(c), by keeping the same parameters but considering a negative wave speed of -8.385, the kink soliton transforms into an anti-kink soliton. Kink and anti-kink solitons are fundamental entities in the domain of nonlinear wave dynamics, manifesting in a variety of physical systems, including fluid dynamics, optical fibers, and condensed matter physics [35, 36]. They serve as representations of topological solitons within the framework of field theory, facilitating the exploration of domain walls and phase transitions. In the realm of plasma physics, they are employed to model energy transport phenomena and nonlinear wave interactions [37, 38]. Optical solitons that are predicated on kink structures are vital for ensuring stable signal transmission within fiber optic systems. Furthermore, these solitons are also observed in biological contexts, such as the dynamics of DNA and the propagation of nerve impulses. The inherent stability and robustness of these solitons render them indispensable for elucidating nonlinear phenomena across a myriad of scientific and engineering disciplines [39,40].

In Figure 3(a)–(c), the wave dynamics of the solution $\Psi_{3b}(\varsigma, \mathfrak{t})$ are depicted using the parameter values $\Upsilon = 2.3$ and $\mathfrak{B} = 0.23$, with the domain of ς and $\mathfrak{t}$ set as $(-7.6, 7.6)$. For a positive wave speed of 8.850, the solution exhibits a right-dark soliton. In Figure 3(b), the same parameter values are used, but with ς fixed at 2.45 to generate a 2D plot. Conversely, in Figure 4(a)–(c), by maintaining the same parameters but considering a negative wave speed of -2, the right-dark soliton transforms into a left-dark soliton [41,42]. Right-dark and left-dark solitons are significant in the study of nonlinear wave dynamics, especially in the contexts of optical fiber communications, Bose-Einstein condensates, and fluid dynamics. Their stability and robustness contribute to their utility in information transmission within optical systems, where they play a critical role in minimizing dispersion and enhancing the integrity of signals [43,44].

In Figure 5(a)–(c), the wave dynamics of the solution $\Psi_{7b}(\varsigma, \mathfrak{t})$ are depicted using the parameter values $\Upsilon = 2.3$ and $\mathfrak{B} = 0.20$, with the domain of ς and $\mathfrak{t}$ set as $(-5.4, 5.4)$. For a positive wave speed of 17.80, the solution exhibits a family of periodic solitons. In Figure 5(b), the same parameter values are used, but with ς fixed at 3.5 to generate a 2D plot. The class of periodic soliton solutions is integral to the comprehension of nonlinear wave propagation across diverse physical systems [45,46]. These solutions depict stable, recurrent wave formations that emerge in integrable and near-integrable models, rendering them indispensable for the exploration of nonlinear dynamics [47,48].

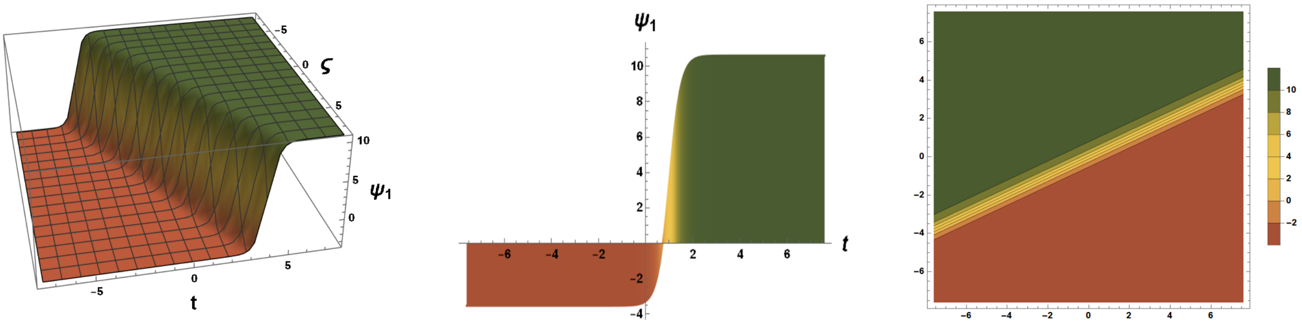

(a) 3D visualization **(b)** 2D visualization **(c)** Contour visualization

Figure 1. Visualization of $\Psi_1(\varsigma, t)$ with positive wave speed, resulting in the emergence of a kink soliton.

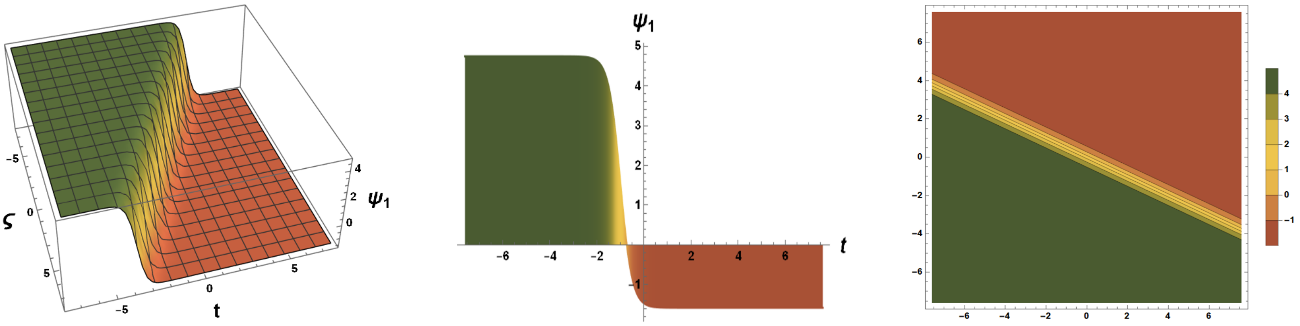

(a) 3D visualization **(b)** 2D visualization **(c)** Contour visualization

Figure 2. Illustration of $\Psi_1(\varsigma, t)$ influenced by a negative wave speed, generating an anti-kink soliton.

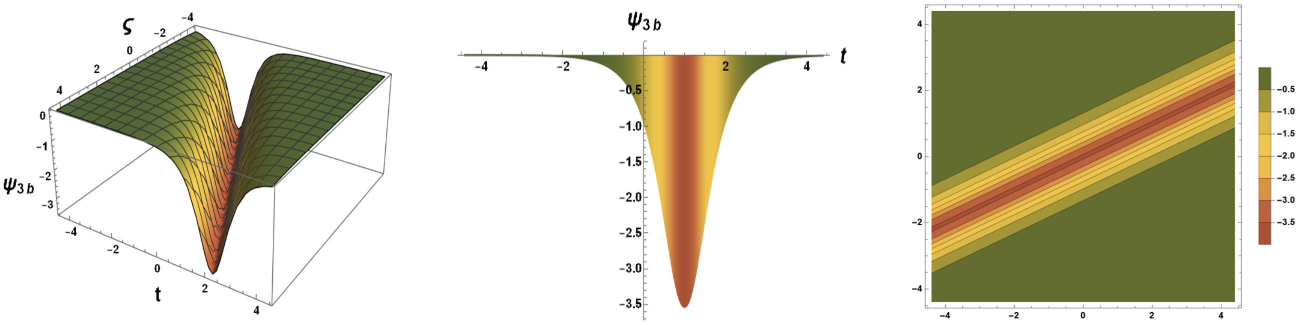

(a) 3D visualization **(b)** 2D visualization **(c)** contour visualization

Figure 3. Representation of $\Psi_{3b}(\varsigma, t)$ under a positive wave speed, forming a right-dark soliton.

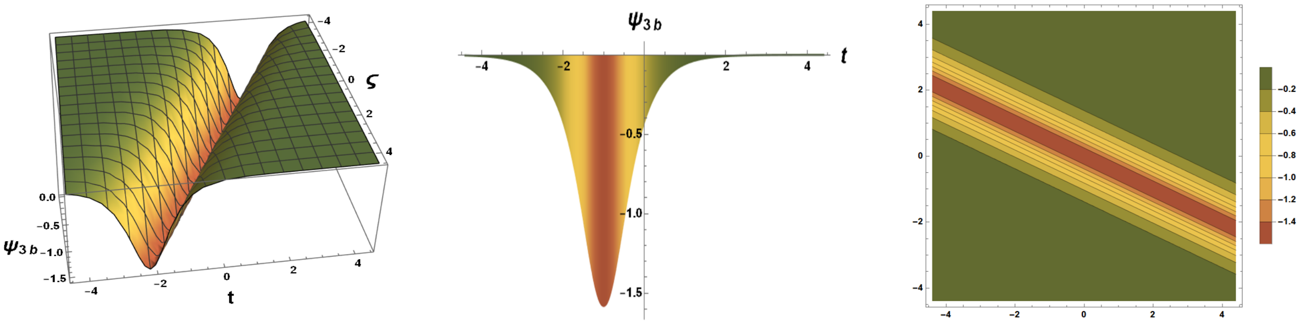

(a) 3D visualization **(b)** 2D visualization **(c)** Contour visualization

Figure 4. Graphical depiction of $\Psi_{3b}(\varsigma, \mathrm{t})$ under a negative wave speed, showcasing a left-dark soliton structure.

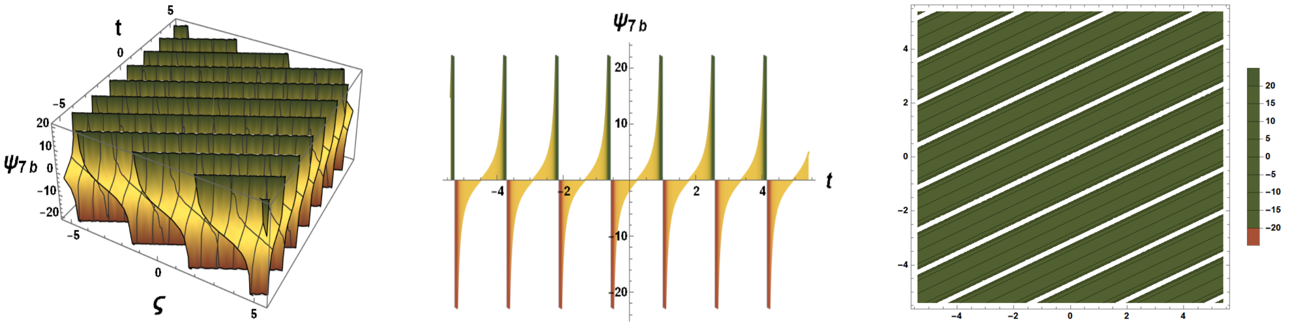

(a) 3D visualization **(b)** 2D visualization **(c)** Contour visualization

Figure 5. Visualization of $\Psi_{7b}(\varsigma, \mathrm{t})$ demonstrating the effect of a positive wave speed, yielding a family of periodic solitons.

6. Characteristics of the dynamic system

In this section, we study the characteristics of the dynamical system using the Hamiltonian function and chaos analysis.

6.1. Hamiltonian function

The analysis of chaotic characteristics involves decomposing Eq (2.21) into a planar system as follows [49]:

$$\begin{cases} \dfrac{d\mathcal{V}}{d\mathcal{R}} = \mathcal{W}, \\ \dfrac{d\mathcal{W}}{d\mathcal{R}} = \dfrac{\kappa \mathcal{V}^3}{30} - \dfrac{\mu_1 \mathcal{V}}{6} + \dfrac{\Upsilon}{6\mathcal{V}} - \dfrac{2\mathcal{W}^2 \mathfrak{B}}{\mathcal{V}} - \dfrac{2\mathcal{W}^2}{\mathcal{V}}, \quad \mathcal{V} \neq \ 0. \end{cases} \tag{6.1}$$

The Hamiltonian condition is:

$$\frac{\partial \mathcal{H}}{\partial \mathcal{W}} = \frac{d\mathcal{V}}{d\mathcal{R}}, \quad \frac{d\mathcal{W}}{d\mathcal{R}} = -\frac{\partial \mathcal{H}}{\partial \mathcal{V}}. \tag{6.2}$$

The Hamiltonian $\mathcal{H}(\mathcal{V},\mathcal{W})$ is derived using Eq (6.2) along with the first equation from the system (6.1), resulting in [50]

$$\frac{\partial\mathcal{H}}{\partial\mathcal{W}} = \mathcal{W}\cdot \tag{6.3}$$

By integrating Eq (6.3) with respect to $\mathcal{W}$, we get

$$\mathcal{H}(\mathcal{V},\mathcal{W}) = \frac{\mathcal{W}^2}{2} + \mathcal{Z}(\mathcal{V}). \tag{6.4}$$

Here, $\mathcal{Z}(\mathcal{V})$ denotes an arbitrary function of $\mathcal{V}$ that needs to be determined. The second equation of the system (6.1) is given by

$$\frac{d\mathcal{W}}{d\mathcal{R}} = \frac{\kappa\mathcal{V}^3}{30} - \frac{\mu_1\mathcal{V}}{6} + \frac{\Upsilon}{6\mathcal{V}} - \frac{2\mathcal{W}^2\mathfrak{B}}{\mathcal{V}} - \frac{2\mathcal{W}^2}{\mathcal{V}}, \quad \mathcal{V} \neq 0. \tag{6.5}$$

Differentiating Eq (6.4) partially with respect to $\mathcal{V}$, we obtain

$$\frac{\partial\mathcal{H}}{\partial\mathcal{V}} = \mathcal{Z}'(\mathcal{V})\cdot \tag{6.6}$$

Substituting Eqs (6.5) and (6.6) into the second condition of Eq (6.2), we obtain

$$-\mathcal{Z}'(\mathcal{V}) = \frac{\kappa\mathcal{V}^3}{30} - \frac{\mu_1\mathcal{V}}{6} + \frac{\Upsilon}{6\mathcal{V}} - \frac{2\mathcal{W}^2\mathfrak{B}}{\mathcal{V}} - \frac{2\mathcal{W}^2}{\mathcal{V}}, \quad \mathcal{V} \neq 0. \tag{6.7}$$

By integrating the equation above with respect to $\mathcal{V}$, the potential energy is obtained

$$\mathcal{Z}(\mathcal{V}) = -\frac{\kappa\mathcal{V}^4}{120} + \frac{\mu_1\mathcal{V}^2}{12} - \frac{\Upsilon\ln(\mathcal{V})}{6} + 2\mathcal{W}^2(\mathfrak{B}+1)\ln(\mathcal{V}), \quad \mathcal{V} \neq 1. \tag{6.8}$$

Thus, the Hamiltonian function is determined as

$$\mathcal{H}(\mathcal{V},\mathcal{W}) = \frac{\mathcal{W}^2}{2} - \frac{\kappa\mathcal{V}^4}{120} + \frac{\mu_1\mathcal{V}^2}{12} - \frac{\Upsilon\ln(\mathcal{V})}{6} + 2\mathcal{W}^2(\mathfrak{B}+1)\ln(\mathcal{V}), \quad \mathcal{V} \neq 1. \tag{6.9}$$

The total derivative of $\mathcal{H}(\mathcal{V},\mathcal{W})$ with respect to $\mathcal{R}$ is expressed as

$$\frac{d\mathcal{H}}{d\mathcal{R}} = \frac{\partial\mathcal{H}}{\partial\mathcal{V}}\frac{d\mathcal{V}}{d\mathcal{R}} + \frac{\partial\mathcal{H}}{d\mathcal{W}}\frac{\partial\mathcal{W}}{d\mathcal{R}}\cdot \tag{6.10}$$

For Hamiltonian conservation, the total derivative must be zero. Since $\frac{d\mathcal{H}}{d\mathcal{R}} \neq 0$, for general parameters, $\mathcal{H}(\mathcal{V},\mathcal{W})$ is not conserved. This non-conservation may arise from non-Hamiltonian behavior or external energy exchange, potentially leading to complex and chaotic dynamics. The regular form of the system (6.1) is given by

$$\begin{cases} \dfrac{d\mathcal{V}}{d\mathcal{R}} = \mathcal{W}, \\ \dfrac{d\mathcal{W}}{d\mathcal{R}} = \dfrac{\kappa\mathcal{V}^3}{30} - \dfrac{\mu_1\mathcal{V}}{6} + \dfrac{\Upsilon}{6\mathcal{V}} - \dfrac{2\mathcal{W}^2(\mathfrak{B}+1)}{\mathcal{V}}, \quad \mathcal{V} \neq 0, \quad \because \quad \dfrac{d\mathcal{W}}{d\mathcal{R}} = -\dfrac{\partial\mathcal{H}}{\partial\mathcal{V}}. \end{cases} \tag{6.11}$$

6.2. *Chaos anaysis*

Nonlinear systems often exhibit chaos due to their irregular and unpredictable evolution, yet they follow deterministic equations. To analyze the chaotic behavior of Eq (6.11), we introduce an external periodic force, $\mathfrak{A}\cos(\mathfrak{S}\mathcal{R})$, and proceed as follows [51]:

$$\begin{cases} \dfrac{d\mathcal{V}}{d\mathcal{R}} = \mathcal{W}, \\ \dfrac{d\mathcal{W}}{d\mathcal{R}} = \dfrac{\kappa\mathcal{V}^3}{30} - \dfrac{\mu_1\mathcal{V}}{6} + \dfrac{\Upsilon}{6\mathcal{V}} - \dfrac{2\mathcal{W}^2(\mathfrak{B}+1)}{\mathcal{V}} + \mathfrak{A}\cos(\mathfrak{S}\mathcal{R}), \quad \mathcal{V} \neq 0. \end{cases} \tag{6.12}$$

Here, $\mathfrak{S}$ represents its frequency, while $\mathfrak{A}$ denotes the amplitude of the external force. Figures 6–9 illustrate the impact of perturbations on the solution's dynamics through 3D and 2D phase portraits, time series representations, and return maps of the system (6.11), considering different cases of μ, Υ, and κ with appropriate values of $\mathfrak{A}$ and $\mathfrak{S}$.

- When $\kappa = 0.28$, $\mu_1 = 4.2$, and $\Upsilon = 0.29$ with $\mathfrak{A} = 0.01, \mathfrak{B} = 0.3$, and $\mathfrak{S} = 2.6$, the system described by Eq (6.12) exhibits chaotic motion, as depicted in Figure 6(a)–(d).
- When $\kappa = 1.33$, $\mu_1 = 0.96$, and $\Upsilon = 0.84$ with $\mathfrak{A} = 0.01, \mathfrak{B} = 0.3$, and $\mathfrak{S} = 1.6$, the system governed by Eq (6.12) displays chaotic behavior, as illustrated in Figure 7(a)–(d).
- When $\kappa = 0.43$, $\mu_1 = 0.16$, and $\Upsilon = -0.24$ with $\mathfrak{A} = 0.01, \mathfrak{B} = 1.3$, and $\mathfrak{S} = 0.56$, the system governed by Eq (6.12) exhibits quasi-periodic motion, as shown in Figure 8(a)–(d).
- When $\kappa = 0.13$, $\mu_1 = 0.36$, and $\Upsilon = -2.44$ with $\mathfrak{A} = 2.01, \mathfrak{B} = 1.3$, and $\mathfrak{S} = 1.56$, the system described by Eq (6.12) demonstrates chaotic behavior, as illustrated in Figure 9(a)–(d).

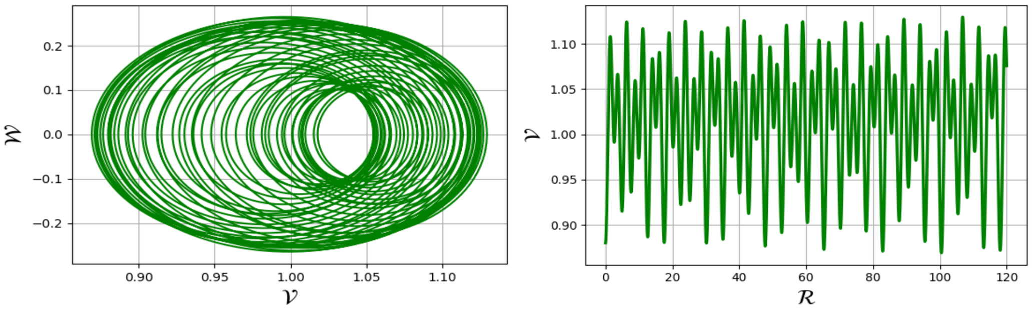

(a) 2D Phase portrait plot **(b)** Time series representation

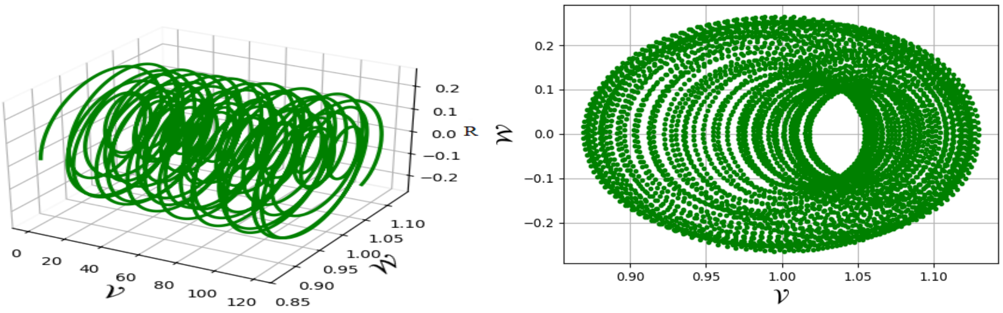

(c) 3D phase portrait plot **(d)** Poincaré map

Figure 6. Illustration of chaotic motion in Eq (6.12) using $\mathfrak{A} = 0.01$ and $\mathfrak{S} = 2.6$.

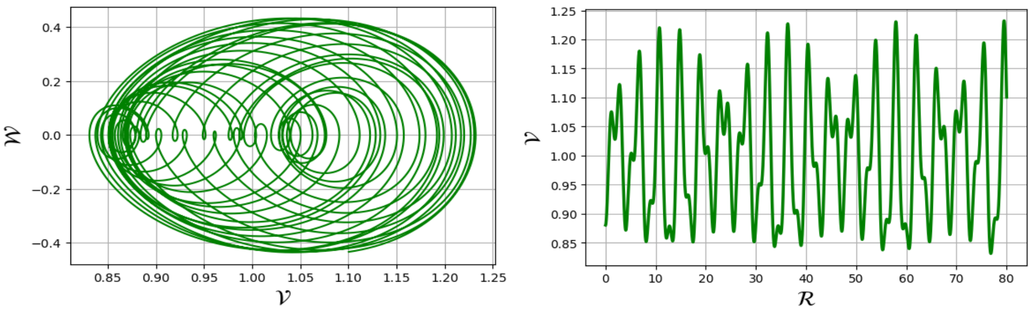

(a) 2D phase portrait plot **(b)** Time series representation

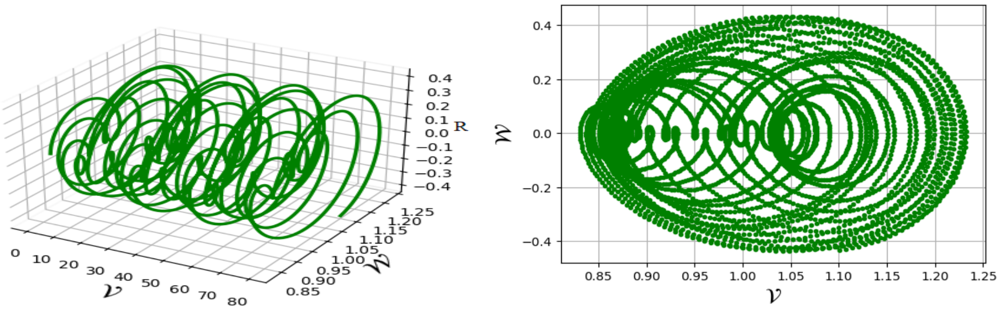

(c) 3D phase portrait plot **(d)** Poincaré map

Figure 7. Illustration of chaotic motion in Eq (6.12) with $\mathfrak{A} = 0.01$ and $\mathfrak{S} = 1.6$.

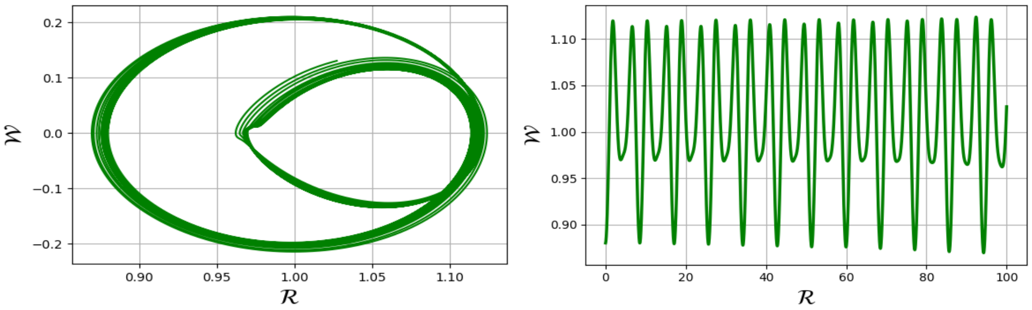

(a) 2D phase portrait plot **(b)** Time series representation

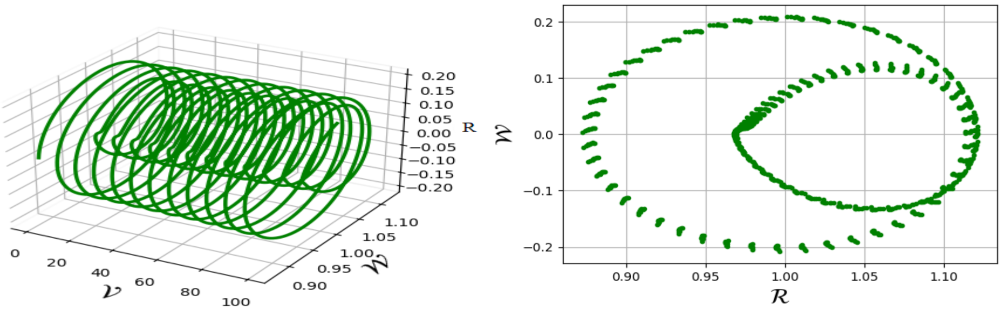

(c) 3D phase portrait plot **(d)** Poincaré map

Figure 8. Illustration of quasi-periodic motion in Eq (6.12) using $\mathfrak{A} = 0.01$ and $\mathfrak{S} = 0.56$.

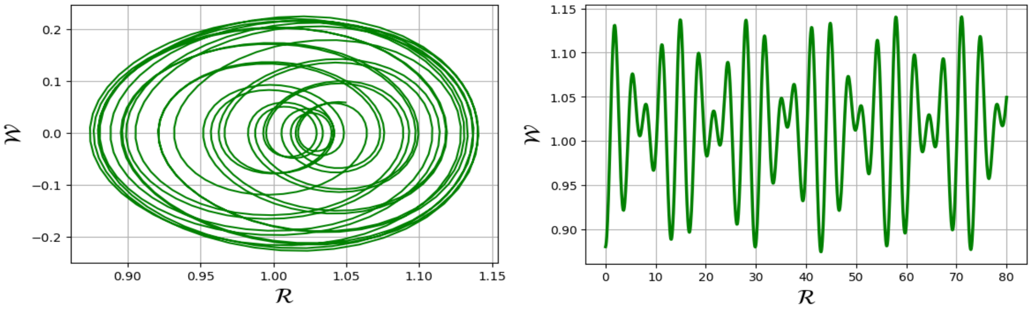

(**a**) 2D phase portrait plot (**b**) Time series representation

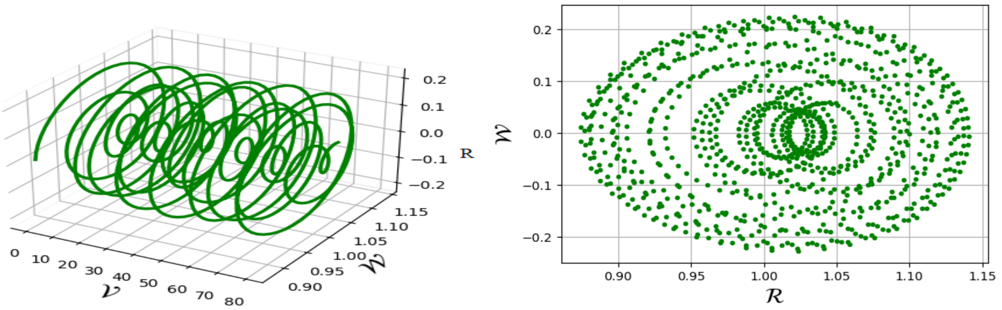

(**c**) 3D phase portrait plot (**d**) Poincaré map

Figure 9. Illustration of chaotic motion in Eq (6.12) using $\mathfrak{A} = 2.01$ and $\mathfrak{S} = 1.56$.

7. Analytical tools for detecting chaos analysis

In this part, we detect chaotic behavior using bifurcation diagrams, Poincaré maps, chaotic attractors, fractal dimensions, and Lyapunov exponents.

7.1. *Return map*

The return map, defined as a plot of $\mathcal{V}(\mathcal{R})$ versus $\mathcal{V}(\mathcal{R}+\zeta)$ with small decay ζ, captures the system's recurrence behavior. In Figure 10, the system is examined for $\mu_1 = 0.33$, $\kappa_2 = 0.76$, $\Upsilon = 0.44$, and $\mathfrak{B} = 0.3$, using different values of $\mathfrak{S}$ and $\mathfrak{A}$. Figure 10(a) shows a spiraling structure that indicates weak chaos with quasi-periodic traces. Figure 10(b) shows closed loops, representing regular periodic motion. In Figure 10(c), a scattered pattern suggests the emergence of chaos. In Figure 10(d), the return map becomes highly irregular, confirming strongly chaotic behavior [54, 55].

7.2. *Bifurcation diagram*

A bifurcation diagram visually represents how the qualitative behavior of a system changes as a parameter varies. It helps identify transitions from periodic to chaotic regimes [53]. Bifurcation diagrams are widely used in nonlinear dynamics to trace critical parameter thresholds leading to chaos in physical, biological, and financial models. Chaotic motion in the system (6.12) is illustrated through the bifurcation diagram for $\mu_1 = 0.33$, $\kappa_2 = 0.76$, and $\Upsilon = 0.44$ with $\mathfrak{A} = 0.01$, $\mathfrak{B} = 0.3$, and $\mathfrak{S} = 1.6$, as shown in Figure 11(a) for two different initial conditions: $(0.55, 0.1)$ in blue color and $(0.88, 0.1)$ in red color.

7.3. Chaotic attractor

Chaotic attractors are bounded, non-repeating trajectories in phase space that exhibit sensitive dependence on the initial conditions. They characterize long-term behavior in chaotic systems [53]. Applications include modeling weather systems, turbulence, and heartbeat rhythms, where deterministic chaos is observed despite apparent randomness. Chaotic motion in the system (6.12) is visualized via chaotic attractors for $\mu_1 = 0.33$, $\kappa_2 = 0.76$, and $\Upsilon = 0.44$, with $\mathfrak{A} = 0.01, \mathfrak{B} = 0.3$, and $\mathfrak{S} = 1.6$, as shown in Figure 11(b).

7.4. Fractal dimensions

Fractal dimensions quantify the complexity of an object by describing how the detail in a pattern changes with the scale at which it is measured [53]. Chaotic systems often exhibit fractal geometry. This measure is used in analyzing strange attractors, pattern formation in nature, and signal complexity in physiological and ecological data. In the system (6.12), the fractal dimensions are used to visualize the dynamics for $\mu_1 = 0.33$, $\kappa_2 = 0.76$, and $\Upsilon = 0.44$, with $\mathfrak{A} = 0.01$, $\mathfrak{B} = 0.3$, and $\mathfrak{S} = 1.6$, as shown in Figure 11(c),(d) for two different initial conditions: $(0.55, 0.1)$ shown in green and $(0.88, 0.1)$ shown in red. The green trajectory exhibits quasi-periodic behavior with a fractal dimension of 1.2, while the red trajectory shows chaotic behavior with a fractal dimension of 5.2.

7.5. Lyapunov exponents

Lyapunov exponents measure the average rates of divergence or convergence of nearby trajectories [53]. A positive Lyapunov exponent indicates chaos. They are crucial in chaos detection, particularly for quantifying sensitivity to the initial conditions in systems like climate models and population dynamics. Chaotic motion in the system (6.12) is illustrated using Lyapunov exponents for the parameters $\mu_1 = 0.33$, $\kappa_2 = 0.76$, and $\Upsilon = 0.44$, with $\mathfrak{A} = 0.01$, $\mathfrak{B} = 0.3$, and $\mathfrak{S} = 1.6$, as shown in Figure 11(d). The computed Lyapunov exponents are $\sigma_1 = 5.312$ and $\sigma_2 = -5.312$. The presence of a positive Lyapunov exponent confirms the chaotic nature of the system.

7.6. Multistability analysis

A dynamic system can exhibit multiple coexisting solutions depending on specific initial conditions and parameter values, a phenomenon known as multistability distribution, which we investigated in our previous research [56]. To analyze this behavior, we examined phase portraits and time series graphs for the system described by Eq (6.12). For validation, we set the parameters as follows: $\mu_1 = 0.33$, $\kappa_2 = 0.76$, and $\Upsilon = 0.44$, with $\mathfrak{A} = 0.31$, $\mathfrak{B} = 1.3$, and $\mathfrak{S} = 1.6$, with the corresponding phase portraits illustrated in Figure 12(a),(b). The trajectories for the initial conditions $(\mathcal{V}, \mathcal{W}) = (0.66, 0.01)$ in green, $(\mathcal{V}, \mathcal{W}) = (0.44, 0.01)$ in red, and $(\mathcal{V}, \mathcal{W}) = (0.22, 0.01)$ in purple initially exhibited chaotic behavior. Similarly, Figure 12(c),(d) presents the results for the parameter values $\mu_1 = 0.33$, $\kappa_2 = 0.76$, and $\Upsilon = 0.44$, with $\mathfrak{A} = 0.01$, $\mathfrak{B} = 0.31$, and $\mathfrak{S} = 5.6$, where two distinct phase portraits were obtained for the initial conditions $(\mathcal{V}, \mathcal{W}) = (0.66, 0.01)$ in green and $(\mathcal{V}, \mathcal{W}) = (0.44, 0.01)$ in red. The system displayed chaotic trajectory behavior for these conditions.

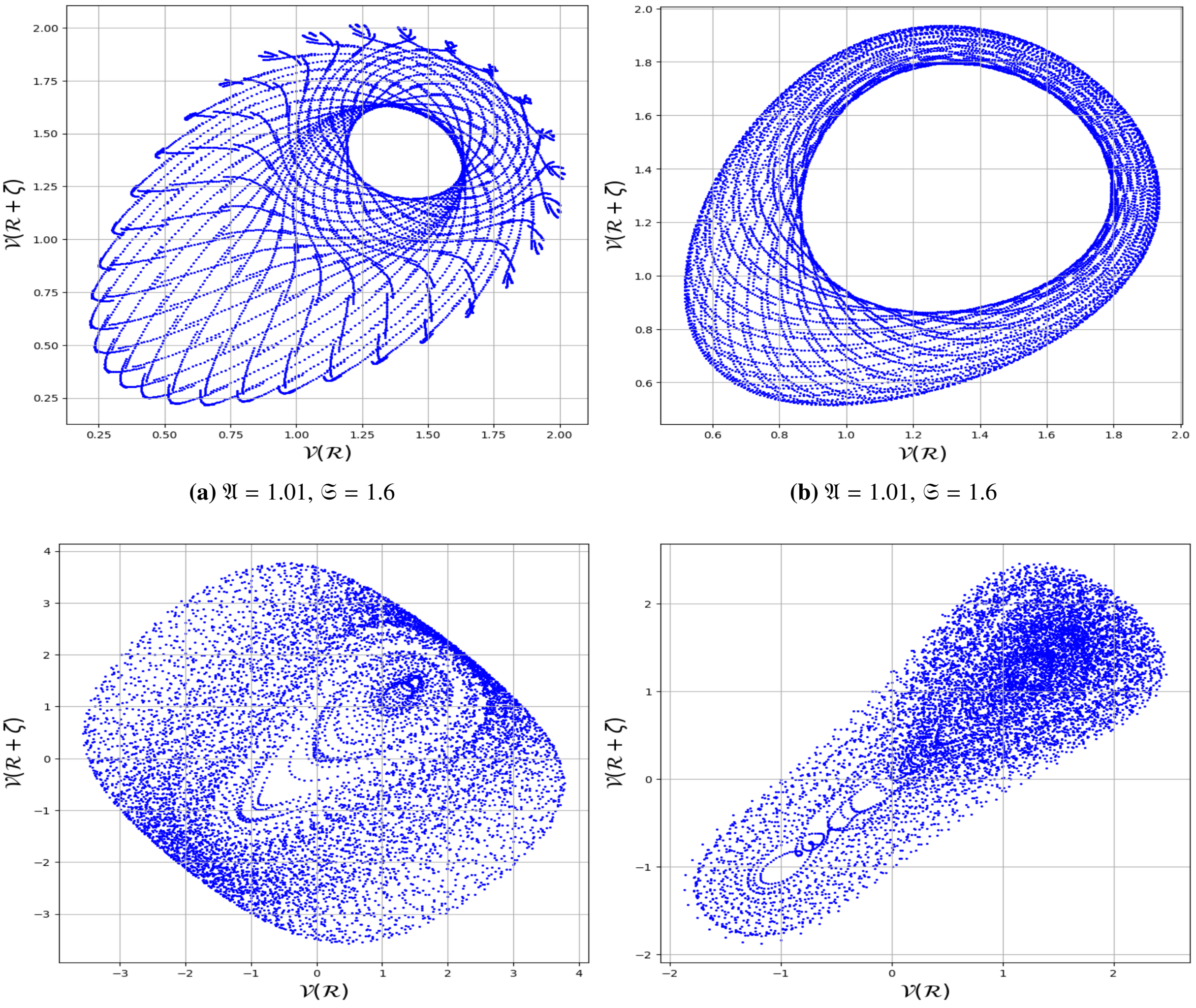

(a) $\mathfrak{A} = 1.01$, $\mathfrak{S} = 1.6$ **(b)** $\mathfrak{A} = 1.01$, $\mathfrak{S} = 1.6$

(c) $\mathfrak{A} = 1.5$, $\mathfrak{S} = 3.20$ **(d)** $\mathfrak{A} = 1.5$, $\mathfrak{S} = 3.20$

Figure 10. Quasi-periodic and chaotic motion of the system (6.12) illustrated using the return map for varying $\mathfrak{A}$ and $\mathfrak{S}$.

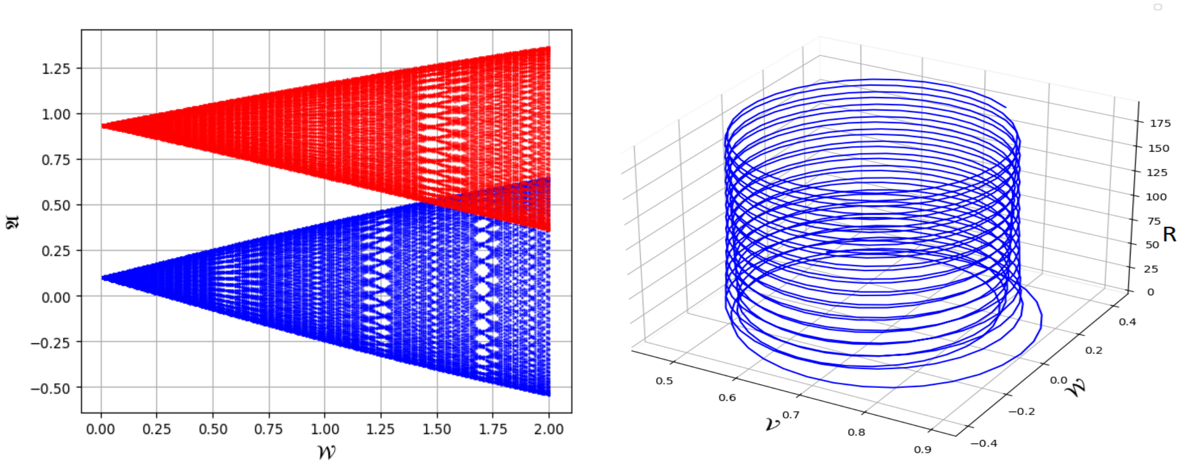

(a) Bifurcation diagram for the parameter $\mathfrak{A}$

(b) Chaotic attractor

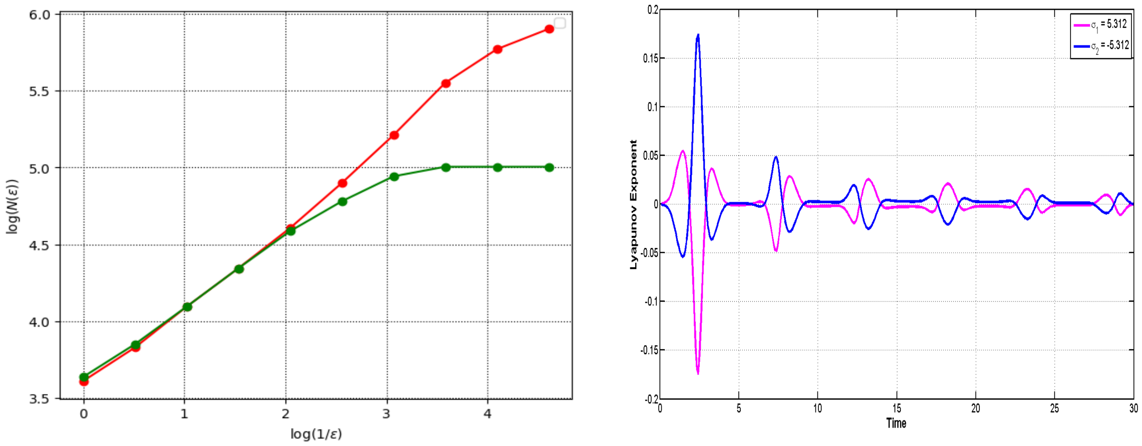

(c) Fractal dimension

(d) Lyapunov exponent

Figure 11. Chaotic motion in the system (6.12) visualized via different computational tools for $\mu_1 = 0.33$, $\kappa_2 = 0.76$, and $\Upsilon = 0.44$, with $\mathfrak{A} = 0.01$, $\mathfrak{B} = 0.3$, and $\mathfrak{S} = 1.6$.

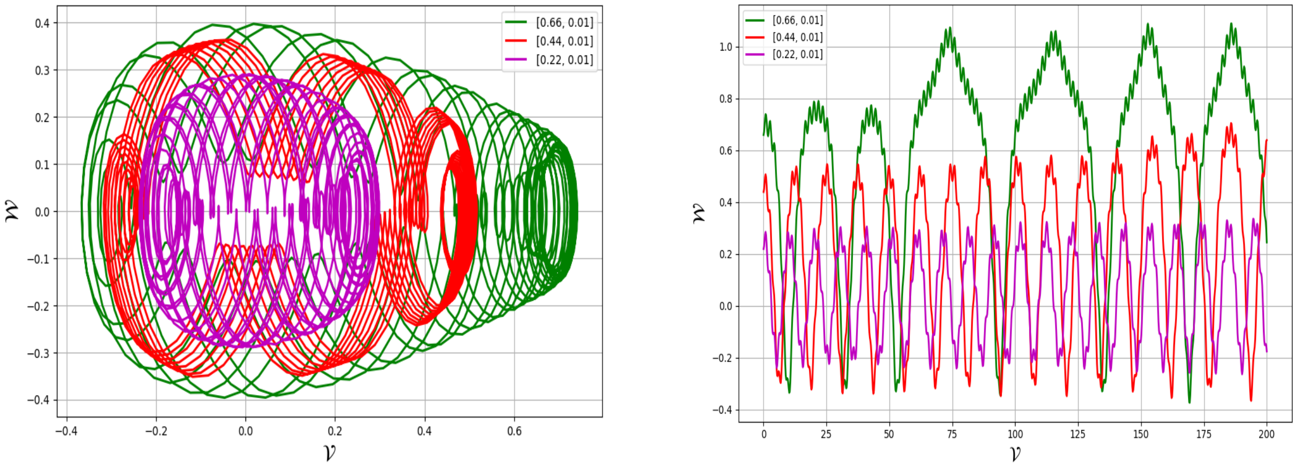

(a) $\mathfrak{A} = 0.31$, $\mathfrak{B} = 1.3$

(b) Time analysis

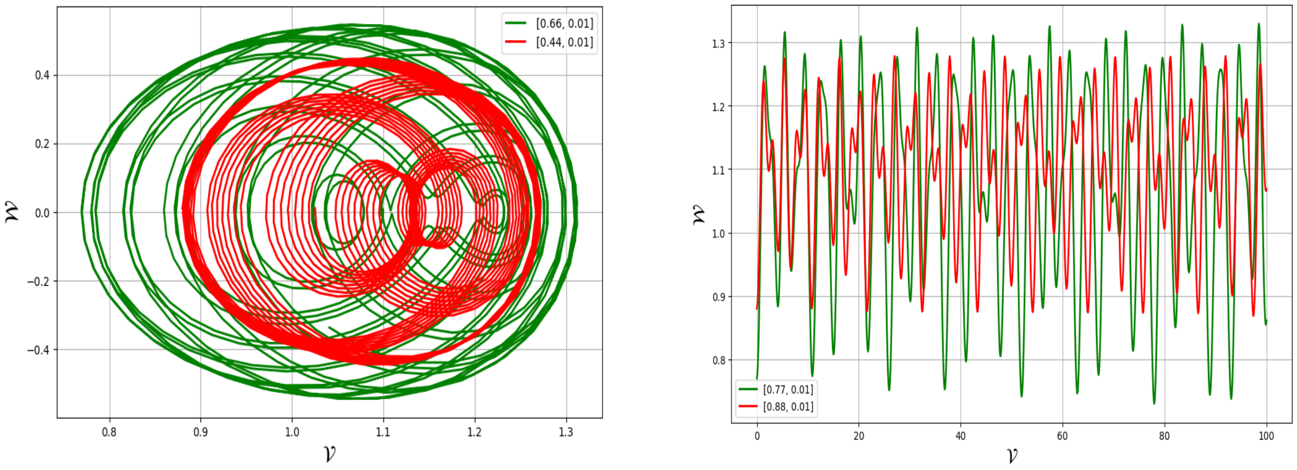

(c) $\mathfrak{A} = 0.31$, $\mathfrak{B} = 5.6$

(d) Time analysis

Figure 12. Chaotic trajectory of the system (6.12) visualized through multistability analysis for $\mu_1 = 0.33$, $\kappa_2 = 0.76$, and $\Upsilon = 0.44$.

8. Conclusions

This study examines specific mathematical equations using analytical techniques, with a particular focus on the generalized ∓ equation, which arises in nonlinear wave propagation across various physical systems, including optics, fluid dynamics, and plasma physics. The symmetry properties of this equation are explored through Lie analysis, where the associated vector fields and Lie groups are determined. Utilizing the optimal system, symmetry reductions are applied, transforming the generalized ∓ equation into a nonlinear ODE. The modified F-expansion method is then employed to derive solitary wave solutions for the reduced equation. To visualize these solutions, graphical representations of selected traveling wave solutions are generated using appropriate parameter values. As a result, various solutions are obtained, including mixed hyperbolic, periodic, mixed periodic, mixed trigonometric, trigonometric, kink singular, anti-kink singular, right-dark singular, left-dark singular, and shock wave solutions, as shown in Figures 1–5. Additionally, the multiplier approach is applied to compute conserved vectors for the generalized ∓ equation. The study further investigates the periodic, quasi-periodic, and chaotic responses of traveling waves under an external periodic disturbance. As the intensity of this disturbance increases, the system transitions from periodic behavior to chaotic dynamics. These complex dynamics were illustrated using time series plots, 2D and 3D phase portraits, return maps, bifurcation diagrams, chaotic attractors, fractal dimensions, poincaré maps, and Lyapunov exponent analysis, as shown in Figures 6–12. All graphs were plotted using Python, which was also utilized to verify the obtained solutions by substituting them back into the original equation. These findings have potential applications in the analytical study of NLPDEs within mathematical physics, plasma physics, applied sciences, nonlinear dynamics, and engineering.

In the future, this study can be extended by exploring lump, breather, and rogue wave solutions, and by incorporating neural networks such as physics-informed neural networks (PINNs) for data-driven modeling. Advanced numerical techniques like the Adomian decomposition method , the variational iteration method, the homotopy perturbation method, and the differential transform method can be employed, along with analytical techniques, to obtain more accurate and diverse results. Additionally, the model can be generalized to include fractional-order dynamics, stochastic perturbations, and symmetry-based reductions, enhancing its applicability to real-world nonlinear systems.

Author contributions

Beenish: Writing-original draft, writing-review and editing, methodology, software, supervision, visualization, conceptualization, investigation, formal analysis; Fehaid Salem Alshammari: Writing-review and editing, project administration, formal analysis, funding acquisition. All authors have read and approved the final version of the manuscript.

Use of Generative-AI tools declaration

The authors declare they have not used artificial intelligence (AI) tools in the creation of this article.

Funding

This work was supported and funded by the Deanship of Scientific Research at Imam Mohammad Ibn Saud Islamic University (IMSIU) (grant number IMSIU-DDRSP2503).

Acknowledgments

The authors extend their appreciation to the Deanship of Scientific Research at Imam Mohammad Ibn Saud Islamic University (IMSIU) for supporting this publication.

Conflict of interest

All authors declare that there are no competing interests.

References

1. I. Alazman, M. N. Mishra, B. S. Alkahtani, M. U. Rahman, Comparative study of novel solitary wave solutions with unveiling bifurcation and chaotic structure modelled by stochastic dynamical system, *Z. Naturforsch. A*, **80** (2025), 285–311. https://doi.org/10.1515/zna-2024-0164
2. T. Han, H. Rezazadeh, M. U. Rahman, High-order solitary waves, fission, hybrid waves and interaction solutions in the nonlinear dissipative (2+1)-dimensional Zabolotskaya-Khokhlov model, *Phys. Scripta*, **99** (2024), 115212. https://doi.org/10.1088/1402-4896/ad7f04
3. T. Alzahrani, M. U. Rahman, Lump, breathing inelastic collision phenomena and rogue wave solutions for a extended KP hierarchy-type equation by neural network-based method, *Ain Shams Eng. J.*, **16** (2025), 103657. https://doi.org/10.1016/j.asej.2025.103657
4. K. Dehingia, S. A. Alharbi, A. J. Alqarni, M. Areshi, M. Alsulami, R. D. Alsemiry, et al., Exploring the combined effect of optimally controlled chemo-stem cell therapy on a fractional-order cancer model, *PloS One*, **20** (2025), e0311822. https://doi.org/10.1371/journal.pone.0311822
5. J. Xu, L. Fan, C. Chen, G. Lu, B. Li, T. Tu, Study on fuel injection stability improvement in marine low-speed dual-fuel engines, *Appl. Therm. Eng.*, **253** (2024), 123729. https://doi.org/10.1016/j.applthermaleng.2024.123729
6. D. Zhang, B. Li, Y. Wei, H. Zhang, G. Lu, L. Fan, et al., Investigation of injection and flow characteristics in an electronic injector featuring a novel control valve, *Energ. Convers. Manage.*, **327** (2025), 119609. https://doi.org/10.1016/j.enconman.2025.119609
7. Z. Chen, Q. Pu, L. Zhu, W. Zhou, Creep behaviour between resilient wheels and rails in a metro system, *Vehicle Syst. Dyn.*, **22** (2025), 1–21. https://doi.org/10.1080/00423114.2025.2494861
8. B. Kopçasız, F. N. K. Sağlam, Exploration of soliton solutions for the Kaup–Newell model using two integration schemes in mathematical physics, *Math. Method. Appl. Sci.*, **48** (2025), 6477–648. https://doi.org/10.1002/mma.10684
9. Beenish, M. Samreen, Bifurcation, multistability, and soliton dynamics in the stochastic potential Korteweg-de vries equation, *Int. J. Theor. Phys.*, **64** (2025), 1–22.
10. M. U. Rahman , L. A. Essa, Explorating the solition solutions of fractional Chen–Lee–Liu equation with birefringent fibers arising in optics and their sensitive analysis, *Opt. Quant. Electron.*, **56** (2024), 1041. https://doi.org/10.1007/s11082-024-06876-9
11. J. Muhammad, U. Younas, E. Hussain, Q. Ali, M. Sediqmal, K. Kedzia, et al., Analysis of fractional solitary wave propagation with parametric effects and qualitative analysis of the modified Korteweg-de Vries-Kadomtsev-Petviashvili equation, *Sci. Rep.*, **14** (2024), 19736. https://doi.org/10.1038/s41598-024-68265-2
12. F. N. Sağlam, B. Kopçasız, K. U. Tariq, Optical solitons and dynamical structures for the zig-zag optical lattices in quantum physics, *Int. J. Theor. Phys.*, **64** (2025), 1–20. https://doi.org/10.1007/s10773-025-05902-0
13. Beenish, E. Hussain, U. Younas, R. Tapdigoglu, M. Garayev, Exploring bifurcation, quasi-periodic patterns, and wave dynamics in an extended Calogero-Bogoyavlenskii-Schiff model with sensitivity analysis, *Int. J. Theor. Phys.*, **65** (2025), 146. https://doi.org/10.1007/s10773-025-06008-3

14. A. Jhangeer, Beenish, Ferroelectric frontiers: Navigating phase portraits, chaos, multistability and sensitivity in thin-film dynamics, *Chaos Soliton. Fract.*, **188** (2024), 115540. https://doi.org/10.1016/j.chaos.2024.115540

15. A. Jhangeer, Beenish, L. Riha, Symmetry analysis, dynamical behavior, and conservation laws of the dual-mode nonlinear fluid model, *Ain Shams Eng. J.*, **16** (2025), 103178. https://doi.org/10.1016/j.asej.2024.103178

16. Beenish, M. Samreen, Exploring quasi-periodic behavior, bifurcation, and traveling wave solutions in the double-chain DNA model, *Chaos Soliton. Fract.*, **192** (2025), 116052. https://doi.org/10.1016/j.chaos.2025.116052

17. Y. Zhou, J. Zhuang, J. Li, Bifurcations and exact traveling wave solutions for the generalized Alexeyev's A∓ equation, *Qual. Theor. Dyn. Syst.*, **24** (2025), 20. https://doi.org/10.1007/s12346-024-01165-y

18. P. E. Hydon, *Symmetry methods for differential equations: A beginner's guide*, Cambridge University Press, 2000. https://doi.org/10.1017/CBO9780511623967

19. D. O. Yali, High-temperature deformation measurement using optical imaging digital image correlation: Status, challenge and future, *Chinese J. Aeronaut.*, **10** (2025), 103472. https://doi.org/10.1016/j.cja.2025.103472

20. S. Yu, Y. Wang, T. Chen, M. Li, X. Zhang , B. Huang, et al., An inclined groove and its optimization design method for improving the energy performance at the saddle zone of axial flow pumps, *Energy*, **10** (2025), 136527. https://doi.org/10.1016/j.energy.2025.136527

21. X. Yin, Y. Lai, X. Zhang, T. Zhang, J. Tian, Y. Du, et al., Targeted sonodynamic therapy platform for holistic integrative Helicobacter pylori therapy, *Adv. Sci.*, **12** (2025), 2408583. https://doi.org/10.1002/advs.202408583

22. W. Bao, H. Liu, F. Wang, J. Du, Y. Wang, H. Li, et al., Keyhole critical failure criteria and variation rule under different thicknesses and multiple materials in K-TIG welding, *J. Manuf. Process.*, **126** (2024), 48–59. https://doi.org/10.1016/j.jmapro.2024.07.093

23. G. Feng, X. Huang, E. Zheng, F. Jiang, Q. Yang, W. Jin, et al., Non-solvent displacement nonaqueous precipitation fabrication of novel foldable HAp ceramic paper without fiber and its performance, *Ceram. Int.*, **50** (2024), 29819–29830. https://doi.org/10.1016/j.ceramint.2024.05.277

24. E. Noether, *Invariante variationsprobleme*, In: Gesammelte Abhandlungen-Collected Papers, Heidelberg, Berlin: Springer, 1983, 231–239. https://doi.org/10.3390/catal15050477

25. E. Noether, Invariant variation problems, *Transport Theor. Stat.*, **1** (1971), 186–207. https://doi.org/10.1080/00411457108231446

26. M. Ruggieri, M. P. Speciale, On the construction of conservation laws: A mixed approach, *J. Math. Phys.*, **58** (2017), 023510. https://doi.org/10.1063/1.4976189

27. J. S. Russell, *Report on waves*, In: Report of the fourteenth meeting of the British Association for the Advancement of Science, **25** (1844).

28. H. H. Zhang, G. G. Yu, Y. Liu, Y. X. Fang, G. Shi, S. Wang, Design of low-SAR mobile phone antenna: Theory and applications, *IEEE T. Antenn. Propag.*, **69** (2020), 698–707. https://doi.org/10.1109/TAP.2020.3016420

29. H. H. Zhang, H. M. Yao, L. Jiang, M. Ng, Enhanced two-step deep-learning approach for electromagnetic-inverse-scattering problems: Frequency extrapolation and scatterer reconstruction, *IEEE T. Antenn. Propag.*, **71** (2022), 1662–1672. https://doi.org/10.1109/TAP.2022.3225532

30. H. H. Zhang, J. B. Chao, Y. W. Wang, Y. Liu, Y. X. Xu, H. Yao, et al., Electromagnetic-thermal co-design of base station antennas with all-metal EBG structures, *IEEE Antenn. Wirel. Pr.*, **22** (2023), 3008–3012. https://doi.org/10.1109/LAWP.2023.3308585

31. Y. Y. Li, Z. W. Zhao, H. H. Zhang, Out-of-core solver based DDM for solving large airborne array, *Appl. Comput. Electrom.*, **31** (2016), 509–515.

32. G. Feng, E. Zheng, F. Jiang, Z. Hu, H. Fu, Y. Li, et al., Group Replacement–Rearrangement-Triggered linear-assembly nonaqueous precipitation synthesis of hydroxyapatite fibers, *ACS Biomater. Sci. Eng.*, **9** (2023), 4597–4606. https://doi.org/10.1021/acsbiomaterials.3c00286

33. B. Li, X. Wang, A. Khurshid, S. F. Saleem, Environmental governance, green finance, and mitigation technologies: Pathways to carbon neutrality in European industrial economies, *Int. J. Environ. Sci. Te.*, **25** (2025), 1–4. https://doi.org/10.1007/s13762-025-06608-w

34. G. Feng, W. Jiang, J. Liu, C. Li, Q. Zhang, L. Miao, et al., Novel nonaqueous precipitation synthesis of alumina powders, *Ceram. Int.*, **243** (2017), 13461–13468. https://doi.org/10.1016/j.ceramint.2017.07.050

35. A. Tian, W. Zhang, J. Hei, Y. Hua, X. Liu, J. Wang, et al., Resistance reduction method for building transmission and distribution systems based on an improved random forest model: A tee case study, *Build. Environ.*, **3** (2025), 113256. https://doi.org/10.1016/j.buildenv.2025.113256

36. X. Sha, X. Si, Y. Zhu, S. Wang, Y. Zhao, Automatic three-dimensional reconstruction of transparent objects with multiple optimization strategies under limited constraints, *Image Vision Comput.*, **24** (2025), 105580. https://doi.org/10.1016/j.imavis.2025.105580

37. S. Lv, H. Liu, F. Wang, X. Liu, M. Peng, Y. Wei, et al., Effect of axial misalignment on the microstructure, mechanical, and corrosion properties of magnetically impelled arc butt welding joint, *Mater. Today Commun.*, **40** (2024), 109866. https://doi.org/10.1016/j.mtcomm.2024.109866

38. J. Fan, X. Zhang, N. He, F. Song, X. Wang, Investigation on novel deep eutectic solvents with high carbon dioxide adsorption performance, *J. Environ. Chem. Eng.*, **3** (2025), 117870. https://doi.org/10.1016/j.jece.2025.117870

39. R. Liu, W. Shen, Data acquisition of exercise and fitness pressure measurement based on artificial intelligence technology, *SLAS Technol.*, **4** (2025), 100328. https://doi.org/10.1016/j.slast.2025.100328

40. W. H. Jiang, Z. Hu, J. M. Liu, Study on low-tanperature synthesis of iron-stabilized aluminium titanate via non-hydrolytic sol-gel method, *J. Syn. Cryst.*, **40** (2011), 465–469.

41. G. Feng, E. Zheng, F. Jiang, Z. Hu, H. Fu, Y. Li, et al., Preparation of novel porous hydroxyapatite

sheets with high Pb^{2+} adsorption properties by self-assembly non-aqueous precipitation method, *Ceram. Int.*, **49** (2023), 30603–20612. https://doi.org/10.1016/j.ceramint.2023.07.013

42. G. Feng, W. Xie, E. Zheng, F. Jiang, Q. Yang, W. Jin, et al., Nonaqueous precipitation combined with intermolecular polycondensation synthesis of novel HAp porous skeleton material and its Pb^{2+} ions removal performance, *Ceram. Int.*, **50** (2024), 19757–19768. https://doi.org/10.1016/j.ceramint.2024.03.099

43. G. Feng, W. Jiang, J. Liu, Q. Zhang, Q. Wu, L. Miao, A novel green nonaqueous sol-gel process for preparation of partially stabilized zirconia nanopowder, *Process. Appl. Ceram.*, **11** (2017), 220–224. https://doi.org/10.2298/PAC1703220F

44. G. Feng, F. Jiang, W. Jiang, J. Liu, Q. Zhang, Q. Wu, et al., Low-temperature preparation of novel stabilized aluminum titanate ceramic fibers via nonhydrolytic sol-gel method through linear self-assembly of precursors, *Ceram. Int.*, **45** (2019), 18704–18709. https://doi.org/10.1016/j.ceramint.2019.06.096

45. X. Zhang, X. Yang, Q. He, Multi-scale systemic risk and spillover networks of commodity markets in the bullish and bearish regimes, *N. Am. J. Econ. Financ.*, **62** (2022), 101766. https://doi.org/10.1016/j.najef.2022.101766

46. X. Zhu, P. Xia, Q. He, Z. Ni, L. Ni, Ensemble classifier design based on perturbation binary salp swarm algorithm for classification, *CMES-Comp. Model. Eng.*, **135** (2023), 653–671. https://doi.org/10.32604/cmes.2022.022985

47. B. Li, H. Liang, Q. He, Multiple and generic bifurcation analysis of a discrete Hindmarsh-Rose model, *Chaos Soliton. Fract.*, **146** (2021), 110856. https://doi.org/10.1016/j.chaos.2021.110856

48. B. Li, Y. Zhang, X. Li, Z. Eskandari, Q. He, Bifurcation analysis and complex dynamics of a Kopel triopoly model, *J. Comput. Appl. Math.*, **426** (2023), 115089. https://doi.org/10.1016/j.cam.2023.115089

49. Beenish, M. Samreen, Analytical solutions and dynamical insights of the modified Benjamin–Bona–Mahony equation with applications in nonlinear optics, *J. Appl. Math. Comput.*, **71** (2025), 699–723. https://doi.org/10.1007/s12190-025-02484-2

50. F. Ali, A. Jhangeer, M. Muddassar, Comprehensive classification of multistability and Lyapunov exponent with multiple dynamics of nonlinear Schrödinger equation, *Nonlinear Dynam.*, **113** (2025), 10335–10364. https://doi.org/10.1007/s11071-024-10781-x

51. Y. Gu, L. Peng, Z. Huang, Y. Lai, Soliton, breather, lump, interaction solutions and chaotic behavior for the (2+1)-dimensional KPSKR equation, *Chaos Soliton. Fract.*, **187** (2024), 115351. https://doi.org/10.1016/j.chaos.2024.115351

52. Beenish, M. Asim, S. Boulaaras, M. U. Rahman, Dynamical behaviour and solutions in the fractional Gross–Pitaevskii model, *Math. Comp. Model. Dyn.*, **31** (2025), 2529190. https://doi.org/10.1080/13873954.2025.2529190

53. Y. Gu, Y. Lai. Analytical investigation of the fractional Klein–Gordon equation along with analysis of bifurcation, sensitivity and chaotic behaviors, *Mod. Phys. Lett. B*, **39** (2025), 2550124. https://doi.org/10.1142/S0217984925501246

54. W. H. Jiang, G. Feng, J. M. Liu, S. Y. Tan, Y. Yu, Preparation of aluminum titanate film by sol-gel method and its fused salt corrosion resistance, *J. Synth. Cryst.*, **39** (2010), 917–921.
55. Q. Fang, Q. Sun, J. Ge, H. Wang, J. Qi, Multidimensional engineering of nanoconfined catalysis: Frontiers in carbon-based energy conversion and utilization, *Catalysts*, **15** (2025), 477. https://doi.org/10.3390/catal15050477
56. A. Khan, F. S. Alshammari, S. Yasin, Beenish, Exact solitary wave solutions and sensitivity analysis of the fractional (3+1)D KdV–ZK equation, *Fractal Fract.*, **9** (2025), 476. https://doi.org/10.3390/fractalfract9070476

AIMS Press